Systematically defining selective autophagy receptor-specific cargo using autophagosome content profiling

Susanne Zellner[1], Martina Schifferer[1, 2], Christian Behrends[1,3]

[1]Munich Cluster for Systems Neurology (SyNergy), Medical Faculty, Ludwig-Maximilians-University München, Feodor-Lynen Strasse 17, 81377 Munich, Germany

[2]German Center for Neurodegenerative Diseases (DZNE), Munich 81377, Germany

[3]Lead contact

Correspondence to: christian.behrends@mail03.med.uni-muenchen.de

SUMMARY

Autophagy deficiency in fed conditions leads to the formation of protein inclusions highlighting the contribution of this lysosomal delivery route to cellular proteostasis. Selective autophagy pathways exist that clear accumulated and aggregated ubiquitinated proteins. Receptors for this type of autophagy (aggrephagy) include p62, NBR1, TOLLIP and OPTN which all possess LC3-interacting regions and ubiquitin-binding domains (UBDs), thus working as a bridge between LC3/GABARAP proteins and ubiquitinated substrates. However, the identity of aggrephagy substrates and the redundancy of aggrephagy and related UBD-containing receptors remains elusive. Here, we combined proximity labeling and organelle enrichment with quantitative proteomics to systematically map the autophagic degradome targeted by UBD-containing receptors under basal and proteostasis challenging conditions in human cell lines. We identified various autophagy substrates, some of which were differentially engulfed by autophagosomal and endosomal membranes via p62 and TOLLIP, respectively. Overall, this resource will allow dissection of autophagy's proteostasis contribution to numerous individual proteins.

KEYWORDS: Autophagy, aggrephagy, selective autophagy receptors, SQSTM1/p62, TOLLIP, autophagosomes, APEX2, proximity labeling, endosomal microautophagy, proteostasis imbalance

INTRODUCTION

Macroautophagy (hereafter autophagy) is a conserved degradation pathway. A broad range of cytosolic constituents including invading pathogens, damaged organelles or parts thereof, aggregated proteins and other macromolecules are enclosed by double-membraned vesicles, coined autophagosomes, and degraded upon their fusion with lysosomes (Mizushima and Komatsu, 2011). Thereby, autophagy essentially contributes to the cellular homeostasis of organelles, proteins and metabolites as well as innate immunity. A hallmark of autophagy is the conjugation of ubiquitin (Ub)-like human ATG8 (hATG8) family members (MAP1LC3A, MAP1LC3B (LC3B), MAP1LC3B2, MAP1LC3C, GABARAP, GABRAPBL1 and GABARAPL2) to phosphatidylethanolamine (PE) in- and outside of incipient autophagosomes (Mizushima et al., 2011). A major function of hATG8-PE is to serve as docking site for regulatory components and selective receptors on the concave site of forming autophagosomes (Birgisdottir et al., 2013). These receptors recognize distinct cargo and tether it to the engulfing autophagosome (Stolz et al., 2014). Selectivity is conferred by two defining components found in all receptors: an LC3-interaction region (LIR) with which the receptors bind to hATG8-PE and a cargo-binding element which can either be transmembrane (TM) segments or protein-protein interaction scaffolds such as the Ub-binding domains (UBDs) (Rogov et al., 2014). Through their UBDs, receptors bind cytosolic bacteria, damaged mitochondria and protein aggregates, all of which are modified with Ub (Kirkin et al., 2009b). Notably, autophagosomal engulfment of cargo can also occur independent of ubiquitin, either through direct or adaptor-mediated binding of receptors to substrate proteins (Jain et al., 2010; Komatsu et al., 2010) or vesicles and organelles (Maejima et al., 2013; Princely Abudu et al., 2019), respectively. Due to their similarities, 6 soluble receptors are grouped together as SQSTM1-like receptors (SLRs) (Deretic, 2012). The funding member of this family of proteins is SQSTM1 (alias p62) which is highly similar to NBR1. Both harbor so-called canonical LIR motifs with a core sequence of $[W/F/Y]_0$-X_1-X_2-$[L/V/I]_3$ (Kirkin et al., 2009a; Pankiv et al., 2007) and interact via their PB1 domains (Lamark et al., 2003). They also share a Ub-associated domain (UBA) and help to clear protein aggregates (Kirkin et al., 2009a; Pankiv et al., 2007) and peroxisomes (Deosaran

et al., 2013; Kim et al., 2008). NDP52 (alias CALCOCO2) and TAX1BP1 have a highly similar domain architecture containing atypical c-type LIRs and Ub-binding zinc fingers (ZFs) (Fu et al., 2018) and eliminate bacteria, mitochondria and aggregates (Fu et al., 2018; Heo et al., 2015; Lazarou et al., 2015; Sarraf et al., 2020; von Muhlinen et al., 2012). OPTN, which serves as SLR in mitophagy, xenophagy and aggrephagy upon its phosphorylation by TBK1 (Heo et al., 2015), carries a LIR (Wild et al., 2011) and two UBDs: a ZF and a UBD in ABIN proteins and NEMO (UBAN) domain (Heo et al., 2015; Korac et al., 2013; Lazarou et al., 2015; Wild et al., 2011). Lastly, the aggrephagy receptor TOLLIP contains a Ub-binding CUE domain and 2 putative LIRs (Lu et al., 2014). However, its role in autophagy is poorly defined. While all SLRs are associated with the clearance of ubiquitinated proteins, the identity of these proteins remains largely elusive. Further, we do not know whether SLRs exclusively target proteins for lysosomal degradation upon proteostasis challenges or also in unperturbed conditions. Finally, the redundancy of SLRs in degrading different proteins is unexplored. To address these questions, we combined proximity labeling with quantitative proteomics to systematically map the protein inventory of autophagosomes in an SLR-specific manner under basal and proteostasis disturbing conditions. We coupled this approach to manipulation of autophagy regulators and complementarily performed neighborhood and organellar proteomics to further explore cargo proteins. We therewith identified potential new autophagy substrates across a broad range of cellular functions and compartments. Using biochemical and cell biological methods, we validated a number of candidates as bona fide autophagy cargo and subsequently demonstrated that some of these are differentially engulfed by autophagosomal and endosomal membranes via p62 and TOLLIP, respectively. In addition, our profiling revealed that only a small fraction of cargo proteins depends on hATG8 and Ub conjugation for their membrane engulfment and that a majority of basal cargo candidates remains unaffected in response to proteostasis perturbations while a substantial amount of additional new proteins is targeted to the autophagy pathway under these conditions.

RESULTS

Establishment of APEX2-SLR cells

To identify cargo in autophagosomes in the proximity of SLRs, we generated a panel of HeLa cells expressing NBR1, NDP52, OPTN, p62, TAX1BP1 or TOLLIP as N-terminal fusion to the engineered peroxidase APEX2 (Hung et al., 2016) and a myc epitope tag (Figure 1A, S1A). myc-APEX2-LC3B expressing cells were used as control. Treatment with biotin-phenol (30 min) and subsequent pulsing with H_2O_2 (1 min) triggers biotinylation of proteins in the proximity to APEX2 fusions. To specifically enrich biotinylated proteins engulfed with our APEX2 baits in autophagosomes following BafilomycinA1 (BafA1) treatment, we incubated cell homogenates with proteinase K which digests all proteins that are not protected by intact membranes (Figure 1A). Immunoblotting confirmed that our APEX2 fusions, biotinylated proteins and endogenous p62 are indeed partly protected from proteinase K, while the cytosolic domain of the TM protein ATG9A, which harbors its antibody epitope, was degraded (Figure 1B). Only when the protective membranes were lysed with Triton X-100, proteinase K completely cleared the homogenates. Confocal microscopy of our cell panel revealed pairwise localization of the APEX2 baits, LC3 and biotin-positive puncta which in turn partially colocalized with the lysosomal marker LAMP1 upon BafA1 treatment and proximity labeling (Figure 1C, S1B). Moreover, all APEX2 fusions generate electron microscopy (EM) contrast on autophagosomal structures when BafA1 treated cells were subjected to post-fixation 3,3-diaminobenzidine (DAB) labeling and H_2O_2 pulsing (Figures 2A). Taken together, these results indicate that the APEX2-SLR chimeras are targeted to autophagosomes where they biotinylate engulfed proteins destined for lysosomal degradation.

Optimization of vesicle content profiling

Prior to cargo profiling of our APEX2-SLR cell lines, we improved the throughput of our approach by implementing tryptic in-solution digests for processing mass spectrometry (MS) samples. To include a specificity control of homogenates treated with proteinase K in the presence of a membrane-lysing detergent, we substituted Triton X-100 with MS-compatible *RAPI*Gest™ which had no effect on the clearance of homogenates by proteinase K (Figure

S2A). To test the modified protocol with an autophagy-unrelated protein, we chose TMEM106B whose C-terminus predominantly locates in endosomes and lysosomes. We generated HeLa cells expressing C-terminally APEX2-tagged TMEM106B (Figure S2B) and subjected them to proximity labeling. TMEM106B-APEX2 and concomitant biotinylated proteins were partially protected from proteinase K (Figure S2C) and biotinylated proteins co-localized with the endosomal and lysosomal markers EEA1 and LAMP1, respectively (Figure S2D). For profiling the content of TMEM106B-positive vesicles, we compared empty and TMEM106B-APEX2 expressing cells treated with DMSO or BafA1/Torin1. Upon proximity labeling, cells were homogenized followed by proteinase K digestion in the absence and presence of *RAPI*Gest™. Proteolyzed material was cleared by centrifugation and samples were subjected to denaturing lysis, streptavidin pulldown, in-solution tryptic digest and MS analysis (Figure S2E). Pearson's correlation coefficients of minimum 0.97 indicated high reproducibility between triplicates (Figure S2F). Upon excluding protease-resistant proteins (found in the proteinase K and *RAPI*Gest™ treated sample; Table S1), statistical analysis revealed a total of 262 proteins that were significantly enriched in the proximity of luminal TMEM106B-APEX2 (Figure S2G; Table S1). Gene ontology (GO) enrichment analysis of TMEM106B proximity candidates shows prominent terms reflecting biogenesis and trafficking of TMEM106B (Figure S2H). Overall, these findings provide independent confirmation that our modified protocol allows the robust identification of proteins enclosed in transient endomembrane vesicles.

SLR-specific autophagosome content profiling under basal autophagy conditions

Next, we subjected triplicates of APEX2-SLRs and -LC3B expressing cells grown in DMSO or BafA1 to the same profiling procedure as described for TMEM106B (Figure 2B). As specificity control, we included 6 additional samples of BafA1-treated APEX2-LC3B expressing cells whose homogenates were incubated with proteinase K and *RAPI*Gest™. Therewith, 181 protease-resistant proteins were identified as potential contaminants and excluded from further analysis (Table S1). With good reproducibility (Figure 2C), we detected between 500 and 900 proteinase K protected and streptavidin enriched proteins with the different APEX2 fusions

(Figure S2I). Statistical analysis identified a total of 279 non-redundant BafA1-sensitive proteins (68 for LC3B, 88 for NBR1, 122 for NDP52, 148 for p62, 19 for OPTN, 51 for TAX1BP1 and 57 for TOLLIP) across the APEX2 baits (Figure 2D-F; Table S1). These proteins were defined as cargo candidates of basal, housekeeping autophagy. Among those proximity profiled by p62 were hATG8s, selective autophagy receptors, autophagy regulators known to be engulfed by autophagosomes (ULK1, RB1CC1), established substrates (KEAP1, FTL) but also several new cargo candidates. Intriguingly, some of these potential substrates have already been implicated in autophagy (TBK1, TNFAIP3, VCP, TBC1D15, UBQLN2, VAPA, VAPB, PRKCI) while others have not been linked to the pathway (PRKAR1A) (Figure 2F). In contrast, APEX2 labeling of TOLLIP unveiled quite different proteins. Apart from NBR1 and p62, the only other autophagy-related protein in TOLLIP's enclosed proximity was TMEM59. Consistent with the role of TOLLIP in coordinating the endosomal compartment (Jongsma et al., 2016) and mediating endocytic trafficking of ubiquitylated cargoes (Katoh et al., 2004; Xiao et al., 2015; Yamakami et al., 2003), we found several proteins involved in these processes (PDCD6IP, PDCD6, HGS, STAM, ITCH, RAB5C). Notably, none of these factors was known to be engulfed by endomembranes. In addition, we detected a number of other lysosomal destined proteins, which have established links to endocytic trafficking (SCAMP3, TFRC, NDFIP1, SLC2A1, ATP1A1, LPL) (Figure 2F). As quality control, we compared our basal cargo candidates to 2 similar proximity proteomics data sets. First, APEX2-LC3B profiling with the current protocol and its earlier version (Le Guerroue et al., 2017) revealed a considerable overlap of 15 proteins whereas 53-56 proteins were uniquely found only with one of the workflows. Importantly, the number of known autophagy-related proteins was by far larger with the improved method (16 vs. 3) (Figure S3A). Second, only very few basal candidates detected with APEX2-LC3B or APEX2-SLRs overlapped with a recent BirA-LC3B MS-based approach on secretory autophagy (Leidal et al., 2020) (Figure S3B), suggesting that we mainly capture autophagosomes en route to lysosomes.

Common and unique features of SLR-specific basal autophagy cargo candidates

Closer inspection of the basal cargo candidates revealed that for each of the APEX2 fusions exept for OPTN and TOLLIP, a majority of the identified proteins were shared with at least one of the other proximity baits, while a smaller portion was uniquely identified with a single bait. For OPTN and TOLLIP, the ratio between unique and shared cargo candidates was about the same (Figure 3A). Examination of the relative overlap of candidates identified by two APEX2 fusions confirmed this trend. OPTN, TOLLIP and TAX1BP1 shared on average the least cargo candidates, while p62, NBR1, NDP52 and to a lesser extent LC3B showed the biggest pairwise overlap (Figure 3B). Autophagy-related proteins found in the overlap between these 4 baits included GABARAPL2, the ferritino- and ER-phagy receptors NCOA4 and CCPG1, the cargo proteins FASN, FTL and KEAP1, as well as the autophagy regulators ATG9A, TBK1, CLTC, RAB1B, RAB5C and RAB7A (Figure S3C). Remarkably, p62 was the only protein detected in all profiling experiments. Analysis of the topology of cargo candidates unveiled that the large majority of cargo candidates identified by APEX2-p62, -NBR1, -NDP52 and -LC3B represented cytosolic soluble or peripheral membrane proteins (PMP) (Figure 3C). In contrast, for APEX2-OPTN, -TAX1BP1 and -TOLLIP the fraction of transmembrane proteins (TMP) and organelle luminal proteins among the cargo candidates increased at the expense of soluble proteins. The GO analysis showed prominent enrichment of cell adherens-, ATP/GTP- and folding-related terms besides the expected autophagosomal and lysosomal associations (Figure 3D). Literature curation of cargo candidates for their involvement in autophagy revealed an even broader presence of proteins with this annotation across all APEX2 baits (Figure 3E). Given that our dataset had minimal overlap with a recent survey of secretory autophagy ((Leidal et al., 2020), Figure S3B), the GO terms exosomal secretion and extracellular vesicles, enriched among TOLLIP cargo candidates, caught our attention (Figure 3D). Manual inspection showed that the majority of proteins with these terms (SDCBP, HGS, STAM, PDCD6IP, SDC4, CLTC, ATP1A1) were actually part of the endosomal machinery and that several additional TOLLIP cargo candidates (ITCH, NDFIP1, PDCD6, SDC2) shared this association (Figure S3C and S3D). Remarkably, a substantial number of cargo candidates found across SLRs and LC3B were small GTPases (Figure 3E). This group of proteins represents an intriguing new type of

potential autophagy substrates, as many cellular processes including formation or maturation of autophagosomes, nutrient signaling, as well as mitochondrial and cytoskeletal dynamics are regulated in a GTP-dependent manner.

Comparison of SLR cargo candidates and proximity partners

Since biotinylation of cargo candidates occurred inside of autophagosomes, we asked which of these proteins were in the proximity of an APEX2 bait prior to their autophagic engulfment. To address this, we subjected our APEX2 fusions to a second-round proximity profiling without proteinase K digestion (Figure S4A). The experiment was carried out with all APEX2-SLRs and -LC3B expressing cells treated with DMSO or BafA1. Additionally, APEX2-LC3B cells grown in the absence of biotin-phenol and empty cells served as controls. Pearson's correlations above 0.9 indicated high replicate reproducibility (Figure S4B). Upon stringent statistical filtering against proteins found in the 2 controls and for BafA1-dependent changes, we identified between 107 and 208 proteins per APEX2 fusion which we considered as proximity partners of one of the 6 SLRs or LC3B (Figure S4C; Table S1). About half of the partners of APEX2-TAX1BP1, -NDP52, -OPTN and -NBR1 showed abundance changes upon BafA1 treatment. While this fraction increased to 61% and 70% for p62 and LC3B, only 32% of the TOLLIP partners were BafA1-sensitive. Interestingly, the majority of BafA1-sensitive proximity partners of p62 increased, while LC3B proximal proteins were largely decreased. In contrast to the basal cargo proteins, the BafA1-sensitive proximity partners were overall not shared among different SLRs or LC3B (Figure S4D) and only a few were found by more than 2 APEX2 baits (Figure S4E). Comparison of proteinase K protected cargo candidates and proximity partners for each APEX2 fusion revealed only a small overlap between these 2 populations (Figure 3F), indicating that additional factors other than SLRs and LC3B may contribute to recruitment of these proteins to enclosing autophagosomes. Conversely, this comparison also highlighted the specificity of SLR-mediated substrate engulfment as proteins featured more prominent among SLRs as proximity partner than as cargo candidate. For instance, SCAMP3 was exclusively found as TOLLIP cargo candidate, however, it was also

present in proximity to TAX1BP1, p62, OPTN and LC3B besides TOLLIP. Likewise, KEAP1, detected as cargo by APEX2-LC3B, -NBR1, -p62 and -NDP52, was additionally found as proximity partner of TAX1BP1 and TOLLIP. This specificity is further underscored by exclusive pairing examples such as ROBO1 and TMEM33 which were only detected as cargo candidates and proximity partners with APEX2-TOLLIP and -LC3B, respectively (Figure 3F and S3D). The fact that a few known substrates (NIPSNAP1, RTN3) were only detected as proximal proteins and that OPTN profiling revealed far more proximity partners than cargo candidates (Figure 3F) highlights that specific signals are required to induce autophagosomal targeting of these factors.

Large-scale autophagy cargo validation through immune isolation of lysosomes

As an independent approach to identify cellular proteins that are delivered to lysosomes via autophagosomes, we performed lysosome immunoprecipitation (LysoIP) (Abu-Remaileh et al., 2017) which is based on the expression of the lysosomal protein TMEM192 as C-terminal fusion to HA (TMEM192-HA) or FLAG (TMEM192-FLAG) epitopes. These constructs were separately introduced in parental, hexa LC3/GABARAP knockout (ATG8-6-KO) (Nguyen et al., 2016) and hexa receptor KO (Rec-6-KO) HeLa cells (Figure S4G). The latter were generated by CRISPR/Cas9-based deletion of TOLLIP in penta receptor KO cells (Lazarou et al., 2015) (Figure S4F). Upon confirming lysosomal localization of TMEM192-HA and -FLAG (Figure S4H), we treated our LysoIP cell panel with BafA1 and immunopurified lysosomes from homogenates prior to denaturing lysis, in-solution tryptic digestion and MS (Figure S4I). Empty parental and TMEM192-FLAG cells were used to control for unspecific background binding. Proteins were detected with Pearson's correlations of ≥0.83 across replicates (Figure S4J). Statistical analysis of empty and TMEM192-HA expressing cells identified 112 significantly enriched proteins in the latter. These lysosomal constituents included peripheral proteins such as LAMTOR1/2/3, TM proteins such as LAMP1/2, NPC1/2 as well as LDLR and the luminal proteins CTSA/C/D/Z, GBA, GGH, GUSB and HEXB (Figure S4K; Table S1). Next, we filtered for proteins that were significantly enriched in parental compared to ATG8-6-KO or Rec-6-KO

TMEM192-HA expressing cells but not in the corresponding TMEM192-FLAG cells (Figure 3G; Table S1). This approach yielded a total of 757 proteins that were altered through either or both KOs. Importantly, 58 of these autophagy-sensitive lysosomal proteins were also identified in our basal autophagosome content profiling (Figure 3H). Among these were cargo candidates identified by distinct APEX2 baits such as VAPA and VAPB (p62), TMEM33 (LC3B), SCAMP3 and PDIA3 (TOLLIP), CKAP4 (NBR1), AFG3L2 (OPTN) and ATP6V0D1 (NDP52) or detected across APEX2 fusions such as LC3B, NCOA4, PLD3, HLA-A, RAB1A, RAB14, RAB5C and RAB7A (Figure 3G, S3C and S3D). Overall, combining LysoIP with systematic genetic autophagy ablation is a valid complementary approach to identify autophagy cargo proteins. The rather small overlap (8%) between proximity profiling and LysoIP can be explained by the fact that LysoIP also enriches for peripheral lysosomal membrane proteins, autophagosomes represent only one lysosomal delivery route and autophagosomal cargo might be gradually degraded before they reach the lysosome.

Selected cargo candidates are membrane protected and localize to lysosomes

To enable an unbiased validation, we selected 25 diverse cargo candidates based on different topologies (soluble, TMP, PMP), identification by single versus numerous APEX2 baits and overlap between proximity and organellar proteomics. First, cell homogenates treated with proteinase K showed that all of the tested cargo candidates were indeed protected from cleavage, whereas the non-degradative hATG8-interacting protein KBTBD7 (Genau et al., 2015) and the cytosolic domains of ATG9A and SLC38A9 which both contain the respective antibody epitope were digested (Figure 4A and S5A). Second, we examined the subcellular distribution of cargo candidates by confocal microscopy and observed that all selected candidates partially colocalized with lysosomes marked by LAMP1 (Figure 4B and S5B). Third, we probed for abundance changes of cargo candidates in response to BafA1 treatment (Figure 4C and S5C) and detected increases in 18 out of the 25 selected cargo candidates while the remaining 7 cargo candidates (TNIP1, VAPA, PDCD6, SCARB1, G6PD, TRAF2, RHEB) did not show any overt changes (Figure 4C and S5C). The fact that the total pool of a given protein

from this latter group was insensitive to blockage of autolysosomal degradation despite being membrane-protected and delivered to lysosomes, may indicate slower lysosomal targeting or transcription/translation kinetics of these candidates which could prevent the build-up of substantial protein levels in the time frame of our BafA1 treatment.

Examining delivery routes of SLR-specific cargo candidates

The fact that endosomal proteins were prominently found together with membrane enclosed TOLLIP called for a closer inspection. As a reference, we chose p62 since its profiling identified most of the known autophagy substrates. We generated clonal TOLLIP and p62 KO HeLa cells (Figure 5A) and performed protease protection assays for cargo candidates identified by APEX2-TOLLIP or -p62. Consistent with our profiling data, protection of the TOLLIP cargo HGS, SCAMP3, ITCH and PDCD6IP was significantly decreased in TOLLIP KO cells while the p62 candidates CCPG1 and VAPB as well as the NBR1 unique candidate SCARB1 were unaffected (Figure 5B and 5D). Conversely, the p62 cargo candidates CCPG1, VAPB, KEAP1, VAPA, STIP1, VCP and ULK1 were substantially less protected in p62 KO cells compared to the exclusive TOLLIP and NBR1 candidates SCAMP3 and SCARB1, respectively (Figure 5C, 5E and S6A). PDCD6 which was profiled by APEX2-p62 and -TOLLIP was also sensitive to both KOs. Importantly, similar results were obtained with a second batch of clonal KO cells (Figure S6B-D). Overall, these findings demonstrate that different cargo candidates require distinct SLRs for their autophagosomal engulfment. The observation that p62 and its interactor NBR1 were both found among TOLLIP's cargo candidates despite the different cargo preferences of TOLLIP and p62 let us examine the subcellular distribution of these 3 SLRs. While TOLLIP colocalized with p62 or NBR1 in several punctuated structures, a substantial part of TOLLIP-positive puncta showed no colocalization (Figure S6E), supporting the notion that autophagosomes are unlikely a homogenous vesicle population but instead differ at least in their enclosed components. Hence, it is plausible that cargo candidates of endosomal origin are engulfed in a different TOLLIP-positive vesicle than p62 and NBR1. Based on this notion, we investigated whether TOLLIP and p62 take different routes to deliver their cargo proteins

to the lysosome. One such alternative might be endosomal microautophagy (Oku and Sakai, 2018). Hence, we probed to what extent TOLLIP and p62 are engaged by endosomal or autophagosomal membranes. Immunofluorescence analysis showed that a large fraction of TOLLIP colocalized with the multivesicular body (MVB) marker CD63 while only very few p62 puncta were also positive for CD63 (Figure 5F). In contrast, p62 but not TOLLIP was found to colocalize with the pre-autophagosomal marker WIPI2 (Figure 5G). Consistently, we observed a prominent CD63 colocalization for the TOLLIP cargo candidates SCAMP3 and HGS whereas the p62 candidates CCPG1 and VAPB did not colocalize with either CD63- or RAB7-positive structures (Figure S6F and S6G). Extended analysis of our APEX2 fusion targets unveiled that NDP52, OPTN, TAX1BP1 and LC3B but not NBR1 showed considerable co-localizations with CD63 (Figure S6H). By revisiting the EM of our APEX2 fusions, we found positively contrasted MVB-like structures for APEX2-TOLLIP, -OPTN and -LC3B whereas these were absent for APEX2-p62, -NBR1, -NDP52 and -TAX1BP1 (Figure 5H and S6I). Thus, distinct SLRs such as TOLLIP and OPTN as well as LC3B are indeed engaging endosomal membranes while other SLRs such as p62 and NBR1 are preferentially not taking this route. While this preference can change in response to starvation conditions for some SLRs such as p62 (Figure S6K) as reported previously (Mejlvang et al., 2018), others like NBR1 seem to be excluded from engaging endosomal membranes (Figure S6K). Intriguingly, hATG8 lipidation was not required to recruit TOLLIP to CD63-positive structures (Figure S6L and S6M) despite the presence of LC3B on endosomal membranes (Figure 5H and S6H). As an alternative approach to probe this differential routing of cargo, we expressed the hyperactive RAB5-Q79L mutant (Stenmark et al., 1994) as mCherry fusion in HeLa cells. In this setting, TOLLIP and its two cargo candidates HGS and ITCH accumulated in giant endosomes whereas this phenotype was not observed for p62 and its cargo candidates CCPG1 and VAPB (Figure 5I). Consistently, we also detected a significant increase in the proteinase K protected fraction of TOLLIP, HGS and ITCH in RAB5-Q79L compared to mock transfected cells. In contrast, p62, its cargo candidates CCPG1 and VAPB and the NBR1-specific cargo SCARB1 showed decreased protease sensitivity upon RAB5-Q79L expression (Figure 5J and 5K). This suggests that the observed

endosomal engulfment is specific for TOLLIP and its cargo candidates. To define TOLLIP-dependent endosomal microautophagy opposed to p62-mediated autophagosomal engulfment, we monitored lysosomal delivery of cargo candidates of these two pathways upon blockage of autophagosome formation. While colocalization of the p62 cargo VAPB with LAMP1 tended to be largely abolished in cells treated with the ULK1 inhibitor MRT68921 (Petherick et al., 2015) (Figure S7A and S7B), depleted of the hVps34 complex component ATG14 (Figure S7C and S7D) or grown in the presence of the hVps34 inhibitor SAR405 (Ronan et al., 2014) (Figure S7E-S7G), the lysosomal localization of the TOLLIP cargo SCAMP3 was unaffected by these conditions (Figure S7B, S7D and S7G). Conversely, disruption of MVBs by depletion of the ESCRT component CHMP4B (Figure S7H), which is required to incorporate LC3B into enlarged RAB5-Q79L endosomes (Figure S7I) (Leidal et al., 2020), trended towards reduced localization of TOLLIP and its cargoes SCAMP3 and ITCH to LAMP1-positive structures but had no overt effect on LAMP1 colocalizations of the non-TOLLIP cargoes VAPB, PRKAR1A, STIP1 and KEAP1 (Figure S7I). Moreover, compromising MVB integrity by the compounds U18666A or GW4869 (Mejlvang et al., 2018; Sahu et al., 2011) significantly abrogated SCAMP3-LAMP1 colocalizations while the distribution of p62 to LAMP1 positive puncta was unchanged (Figure S8A). In sum, these experiments established that TOLLIP can funnel cargo candidates to lysosomes via endosomal microautophagy while p62 largely mediates engulfment of proteins by incipient autophagosomal membranes.

Defining molecular requirements of cargo engulfment

Since SLRs are sought to serve as molecular bridges between hATG8-PE conjugates in autophagosomal membranes and ubiquitinated substrates, we decided to determine to what extent cargo engulfment depends on these two defining features. For this purpose, we employed 2 inhibitors, ATG8-E1 and Ub-E1, which specifically block the activities of the E1 enzymes for hATG8s and Ub, ATG7 and UBA1, respectively. Immunoblotting for Ub and LC3B confirmed that ATG8-E1 treatment blocked hATG8-PE conjugate formation while incubation with Ub-E1 ablated polyubiquitination (Figure 6A and S6L). Importantly, both inhibitors did not

substantially alter the protease protected fraction of different SLRs or LC3, while the total levels of unconjugated LC3B markedly increased upon ATG8-E1 treatment (Figure S8B). Next, we performed autophagosome content profiling of our APEX2 fusion cells differentially treated with Ub-E1 or ATG8-E1 (Figure 6B, left panel). Triplicate samples were processed for each APEX2 fusion and treatment, while protease-resistant proteins were removed. On average, we identified 582 proteins with high Pearson's correlations (Figure 6C and S8C; Table S1). For data processing, we focused on those proteins that we previously identified as basal cargo candidates (S3C and S3D), of which the overall majority was found in the ATG8-E1 and Ub-E1 datasets (Figure 6D). Statistical analysis revealed that engulfment of a surprisingly small fraction (≤12%) of SLR cargo candidates depends on hATG8 lipidation. For APEX2-LC3B, we observed a decrease for the known LIR-containing proteins CCPG1, TBC1D15 and CALCOCO1 in response to ATG7 inhibition (Figure 6E), consistent with the notion that autophagosomal recruitment of these proteins involves their LIR-dependent docking to hATG8-PE conjugates on incipient autophagosomes. In addition, several cargo candidates in APEX2-LC3B showed clear dependency on active ATG7 including TNIP1, TMEM33, KRT2, PRKAR1A and DNM1L (Figure 6E and 6F), implying possible LIRs in these proteins. We also detected lower amounts of the known substrates KEAP1 and TRAF3 as well as GABARAPL2 (Figure 6E). Since membrane-protected unconjugated LC3B levels were unchanged (Figure S8B), we speculate that the decrease in GABARAPL2 might be due to the reduced engulfment of LIR-containing proteins, which in turn could recruit other hATG8 family members. Intriguingly, the abundance of the ferritinophagy cargo FTL was reduced, while its dedicated receptor NCOA4 did not show sensitivity to ATG7 inhibition (Figure 6E). This could suggest possible redundancy with other ferritinophagy-mediating factors. Some of the LC3B profiled candidates were also found decreased following ATG8-E1 treatment in APEX2-NBR1 (CCPG1, PRKAR1A, DNM1L), -p62 (KEAP1, TRAF3, TNIP1) and -NDP52 (CALCOCO1, KEAP1) samples (Figure 6E), indicating that lipidated LC3B cooperates with NBR1, p62 and NDP52 in the engulfment of these proteins. While ATG7 inhibition decreased several other proteins sampled by APEX2-p62, the treatment had the opposite effect on numerous NDP52

cargo candidates (Figure 6E). Remarkably, a differential effect on cargo engulfment was also observed upon acute inhibition of ubiquitination. Here, 40-60% of the candidates found by APEX2-LC3B and -NBR1, among them CCPG1, RAB7A and FASN, increased while the opposite was true for 17-33% of the TAX1BP1-, NDP52-, p62-, OPTN- and TOLLIP-dependent profiling (Figure 6E and 6F). This surprising result suggests that the role of Ub in autophagic cargo engulfment is likely to go beyond the established eat-me signaling. Next, we extended our analysis to proteins that were not found among the basal cargo candidates but increased upon ATG8-E1 or Ub-E1 treatment (marked new) (Figure 6D). While almost every APEX2 bait yielded some additional proteins in response to either inhibitor, this effect was pronounced with APEX2-LC3B, -NBR1 and -TOLLIP when cells were treated with Ub-E1 and with APEX2-OPTN and -NDP52 when cells were grown in the presence of ATG8-E1 (Figure 6D). While most of the new cargo candidates associated with GO terms of the basal dataset, some of the inhibitor-induced proteins found with NBR1, NDP52 and LC3B fell into mitochondria- or ER-related new categories (Figure 6G). Notably, among those detected with APEX2-LC3B upon Ub-E1 treatment were CCPG1, ATL3, SEC62 and VAPA (Figure 6E and S8D), implicating that acute inhibition of ubiquitination might induce ER-phagy. Complementary to defining cargo dependencies on Ub and hATG8 conjugation, we asked which candidates required one or more members of the SLR family for their enclosure. Thereto, we performed APEX2-LC3B profiling in parental and Rec-6-KO cells (Figure 6B, right panel). With high reproducibility between triplicates, we identified 444 proteins after removal of protease-resistant contaminants (Figure 6H; Table S1). Remarkably, almost half of the profiled proteins were depleted or lost in protected membranes when cells lacked all SLRs (Figure 6I). These proteins included known autophagy machinery and substrates but also several of our validated cargo candidates (SCAMP3, RAB5C, PDCD6IP, GNB2L1, PRKAR1A, RHOA) (Figure 6J and 6K). In fact, many of the LC3B profiled cargo candidates with sensitivities towards ATG8-E1 or Ub-E1 also showed a requirement for the SLR family, confirming the interdependence between receptors and hATG8 or Ub conjugation. An exception was TMEM33 whose engulfment was unaffected in Rec-6-KO cells (Figure 6L), which validates its exclusive LC3B targeting.

Determining SLR-specific degradome alterations upon proteostasis challenges

Finally, we sought to explore how autophagy cargo changes when the cellular proteostasis is perturbed. For this purpose, we selected three conditions: (i) inhibition of translational initiation by puromycin (Puro), (ii) blockage of proteasomal degradation by Bortezomib (Btz) and (iii) expression of an aggregation-prone protein. For the latter, we selected the amyotrophic lateral sclerosis (ALS)-associated, *C9orf72*-derived dipeptide repeat protein poly-GA (Mori et al., 2013) of which 175 repeats were fused to GFP (GA_{175}-GFP). Expression of GFP alone or mock transfections served as controls. As expected, all three conditions led to the build-up of protein inclusions (Figure 7A, 7B, S8E and S9A). The panel of APEX2 baits was found to partially colocalize with Ub-positive structures and LAMP1-positive puncta in HeLa cells treated with Btz or Puro (Figure 7A and S9A). Likewise, SLRs and LC3B partitioned between a punctuated distribution and colocalization with approximately one star-like aggregate per GA_{175}-GFP expressing HEK293T cell without showing alterations at the total protein levels (Figure 7B, S8E and S8F). All three conditions did not overtly alter the proteinase K sensitivity of SLRs and LC3B (Figure S9B). Together, this indicates that SLRs and LC3B are not prominently trapped in inclusions but retain the functionality of being engulfed by endomembranes. Next, we performed proximity profiling under these 3 conditions using our APEX2 fusions (Figure 7C). After protease-resistant contaminants subtraction (Table S1), we obtained a total list of 752 and 1389 proteins for the datasets of Btz/Puro and GA_{175}, respectively, with high replicate reproducibility (Figure 7D and S8G; Table S1). As before, we used the basal cargo candidates as reference and focused the statistical analysis of the Btz, Puro and GA_{175} datasets on these proteins (Figure 7E). Across the challenges, the degradome changes were remarkably small (on average 24%) and different between APEX2 fusions. For example, the fraction of altered basal cargo candidates in LC3B predominantly showed increases in all 3 conditions, while for NBR1 and TOLLIP the opposite effect was observed in 2 conditions. p62, NDP52, TAX1BP1 and OPTN revealed mixed responses to the challenges (Figure 7E). For LC3B, NDP52, p62, TAX1BP1 and TOLLIP, there was almost no overlap between GA_{175} and Btz or Puro while Btz

and Puro similarly altered several proteins of which CALCOCO1, LPL, TNIP1, SDC2 and SDC4 were shared between two of these baits (Figure 7F). In contrast, NBR1 profiling detected Btz and GA_{175} induced decreases in a group of common proteins including CCPG1, DYNC1H1, CLTC, RAB14, PRKAR1A, YWHAE (Figure 7F). Extending the analysis to cargo proteins that were exclusively detected under proteotoxicity conditions (marked new) likewise revealed a heterogenous pattern. GA_{175} and Btz induced most prominent changes profiled by APEX2-LC3B and -p62, while APEX2-NDP52 and -TOLLIP or APEX2-NBR1 and -TAX1BP1 were only affected by GA_{175} or Btz, respectively (Figure 7E). Consistent with these bait and treatment specific differences, less than half of the overall significantly altered proteins were found shared among 2 APEX2 fusions (Figure S9C). The proteotoxicity-induced new cargo was mostly associated with GO terms that were already present in the basal dataset, though exceptions were translation and RNA binding common to NBR1 and p62 upon Btz treatment and ER in LC3B following GA_{175} expression (Figure 7G). The facts that this latter GO term was also found among LC3B cargo following UBA1 inhibition (Figure 6G) and that the ER-phagy factor VAPA (Nthiga et al., 2020) was in the overlap of both treatments (Figure S8H), indicate that GA_{175} aggregation and acute inhibition of ubiquitination converge on inducing ER-phagy. Together, these findings highlight that proteostasis challenges do not induce autophagosomal content alterations at the expense of proteins engulfed in unperturbed conditions. Instead different SLRs mediate the autophagic engulfment of a larger but heterogenous population of cellular proteins in response to proteostasis perturbation.

DISCUSSION

In this study, we used limited proteolysis enhanced spatial proximity proteomics to profile autophagosome content under unperturbed fed conditions in a manner dependent on 6 different SLRs, ubiquitination and LC3/GABARAP lipidation as well as in response to 3 different proteostasis perturbing conditions. This tour de force identified numerous cargo candidates with diverse cellular functions, protein topologies and disease relevance. Using organellar

proteomics, biochemical and cell biological approaches we exemplarily validated a broad spectrum of cargo candidates as bona fide autophagy substrates.

On one hand, this resource provides a broad basis for further analyzing autophagosomal degradation of new cargo. In this context, the family of small GTPases is most intriguing. While members of this broad protein family have been found in autophagosomal preparations before (Heo et al., 2019; Mancias et al., 2014), they were generally not implicated as substrates but instead as regulators of autophagosome-lysosome tethering or fusion. However, the fact that several members of different GTPase subfamilies (RAB5C, RAB7A, RHOA, SAR1B, RHEB) were found membrane protected in several independent experimental settings strongly argues for an autophagic engulfment of these proteins. Whether these GTPases are regulated by autophagy possibly reflecting feedback mechanisms to their roles in mediating membrane dynamics (Langemeyer et al., 2018) or whether some of them are engulfed in a bystander manner, while mediating functions at the closing autophagosomes remain to be explored.

On the other hand, our data set contains a number of surprising mechanistic implications. First, all selective autophagy receptors of the SLR family were enclosed together with a partially overlapping but distinct set of cellular proteins in fed cells. This raises the question to what extent proteins are turned over in a bulk nonselective manner under basal housekeeping conditions. Second, engulfment of cargo was largely independent of LC3/GABARAP lipidation and ubiquitination, two defining features of UBD-containing selective autophagy receptors, but required at least one member of the SLRs family. This suggests that SLRs might be mainly involved in organizing or scaffolding membrane engulfment rather than actively recruiting cargo to incipient autophagosomes. Consistent with this notion, we found only a relatively small overlap between cargo candidates and proximity partners of all SLR family members. Third, induction of protein (co-)aggregation by translation inhibition, proteasome blockage or expression of an aggregation-prone protein overall led to only moderate changes in the autophagosome content sampled by different SLR members. This supports the view that the cell's immediate response to aggregation promoting conditions is to facilitate coalescence of misfolded and aggregated proteins in aggresomes, wherefrom they are cleared by

proteasomes or autophagy once the cell's proteostasis has been re-established (Hipp et al., 2019). Forth, proteasomal substrates do not seem to be diverted to autophagosomal degradation in large numbers when the proteasome is inhibited. The fact that expression of poly-GA was shown to also block the proteasome (Guo et al., 2018) independently confirms this conclusion. Fifth, similar autophagosome content changes induced by different cellular stressors might indicate common autophagic responses as observed with acute ubiquitination inhibition and poly-GA expression which both seem to trigger ER-phagy. While both conditions are known to induce ER stress (Hyer et al., 2018; Nishitoh et al., 2008), the mechanistic basis for this convergence on autophagy requires further examination. Sixth, unbiased sampling of proteins in the proximity of membrane enclosed SLRs unveiled that these receptors mediate differential cytosolic cargo engulfment by endosomal and autophagosomal membranes en route towards lysosomes. Findings from different experiments show that, in contrast to the p62-dependent canonical autophagy substrates CCPG1 and VAPA/B, TOLLIP exclusively facilitates endosomal microautophagy of its cargo proteins HGS, SCAMP3 and ITCH under fed conditions (Figure 7H). This process seemed to be dependent on Ub but independent on ULK1 and hVps34. However, the full molecular requirements of TOLLIP mediated endosomal microautophagy need to be tested in more details. While it remains to be determined whether this process occurs intentionally or as a bystander product of endocytic cargo sorting, the fact that endosomal microautophagy of a number of selective autophagy receptors and their potential substrates has been reported following starvation (Mejlvang et al., 2018), argues against the latter scenario. Given that we also observed OPTN and LC3B at endosomal membranes while hATG8 lipidation was dispensable for endosomal TOLLIP recruitment, further experiments are required to determine the roles of OPTN and hATG8s in endosomal microautophagy. Since we detected TOLLIP-positive autophagosomes by EM, TOLLIP might partition between different autophagy pathways in addition to its endosome- and MDV-associated functions (Jongsma et al., 2016; Ryan et al., 2020). Thus, it will be important to understand the cross-regulation of these multiple vesicle trafficking pathways.

Limitations

While advancing our knowledge on cargo proteins led to deduction of basic principles and expansion of the diversity in the autophagy system, our proximity and organellar proteomic approaches have certain inherent caveats. Most importantly, they relied on overexpression of enzyme or epitope tagged bait proteins whose subcellular localization or molecular interaction might partially differ from those of the untagged endogenous counterparts. As a consequence, a number of proximity labeled or immune isolated proteins might be false positive or differentially responsive to perturbations. Conversely, proteins with a proteinase K resistant conformation (e.g. due to RNA or lipid binding) might have been erroneously excluded from the analysis as background contaminants. Furthermore, cell line and stimuli specific cargo candidates, proximity partners or endolysosomal proteins might have been missed due to the limited use of cell lines and growth conditions. Lastly, while the identification of TOLLIP as endosomal microautophagy receptor exemplified the utility of our SLR cargo resource, much more mechanistic work is required to fully understand the machinery and the signals that drive this alternative lysosomal delivery route.

ACKNOWLEDGEMENTS

We thank Michael Lazarou and Dieter Edbauer for sharing ATG8-6-KO, pentaKO and GA_{175}-GFP cells, Kerstin Karg for EM assistance, Karsten Nalbach for collaborative establishment of MS and EM protocols, Alexander Siebert for providing pHAGE-N-APEX2 and members of the Behrends, Edbauer and Capell labs for critical discussions and readily sharing reagents. This work was supported by the Deutsche Forschungsgemeinschaft (DFG, German Research Foundation) within the frameworks of the Munich Cluster for Systems Neurology (EXC 2145 SyNergy – ID 390857198) and of the Collaborative Research Center 1177 (ID 259130777).

AUTHOR CONTRIBUTIONS

S.Z. performed all experiments except electron microscopy which was conducted by M.S.. All authors participated in data analysis and discussion. S.Z. and C.B. conceived the study and wrote the manuscript.

COMPETING INTERESTS

The authors declare that they have no conflict of interest.

MAIN FIGURES

Figure 1. Autophagosome targeting of APEX2 fused to SLRs

(A) APEX2-based proximity labeling workflow for LC3B and SLRs. (B,C) APEX2 bait expressing HeLa cells were treated for 2 h with BafA1, 30 min with biotin-phenol and 1 min with H_2O_2 followed by homogenization (B) or fixation (C). Homogenates were incubated with proteinase K, Triton X-100 or both and immunoblotted for APEX, biotin, p62 and ATG9. The latter two served as controls (B). Fixed cells were stained for myc, biotin and LAMP1 (C). Scale bars, 10 µm. Co-localization events are indicated by blue and yellow arrowheads. Insets show co-localizations of yellow arrowheads. See also Figure S1.

Figure 2. Identification of protease protected autophagy cargo candidates of SLRs

(A) Electron micrographs of BafA1-treated APEX2-SLRs and -LC3B HeLa cells. Following fixation, cells were incubated with DAB and H_2O_2 prior to standard embedding and ultrathin sectioning. Scale bars, 1 µm. (B) Workflow for APEX2 based autophagosome content profiling. (C) Pearson's correlation of 3 biological experiments depicted in (B). (D) Bar graph of membrane-protected and streptavidin-enriched proteins identified by indicated APEX2 fusions in DMSO and BafA1 treated HeLa cells. The fraction of proteins whose abundance increased upon BafA1 treatment is marked in orange as BafA1 sensitive. (E, F) Volcano plots of proteins from (D) labeled by APEX2-LC3B (E) or -SLRs (F). Cargo candidates that are significantly enriched in the proximity of APEX2 baits in response to BafA1 treatment are highlighted in

orange (p-value ≤ 0.05, student's *t*-test). Known autophagy components are shown in italic. See also Figure S2.

Figure 3. Comparison of SLR cargo candidates and proximity partners

(A) Numbers of shared and unique cargo candidates identified by indicated APEX2 baits. (B) Percent of pairwise overlap of identified cargo candidates between SLRs. (C) Percent of candidates with different protein topologies per APEX2 bait. Soluble, cytosolic protein; TMP, transmembrane protein; PMP, peripheral membrane protein; luminal, protein localized to an organelle lumen. (D) GO term enrichment (FDR≤0.05) of cargo candidates. BP, biological process, CC, cellular component, MF, molecular function. (E) Clustering of cargo candidates according to selected GO terms from D and literature curation. (F) Comparison of cargo candidates and proximity partners of SLRs and LC3B identified by differential protease protection mediated proximity proteomics in HeLa cells. Overlapping proteins and selected proximity partners are displayed in boxes and known bait interactors are marked italic. (G) Volcano plots of proteins found in LysoIPs with TMEM192-HA from Rec-6-KO or ATG8-6-KO cells compared to parental HeLa cells. Significantly decreased proteins in the KOs are marked blue (p-value ≤ 0.05, student's *t*-test). (H) Combined overlap between significantly decreased proteins from G and basal cargo candidates. See also Figure S3 and S4.

Figure 4. Validation of SLR cargo candidates

(A,B) BafA1-treated HeLa cells were homogenized (A) or fixed (B). Homogenates were incubated with proteinase K, Triton X-100 or both and immunoblotted with indicated antibodies. ATG9 and KBTBD7 served as negative controls (A). Fixed cells were stained with indicated antibodies and DAPI (B). Scale bars, 10 µm. Co-localization events are indicated by blue and yellow arrowheads. Insets show co-localizations of yellow arrowheads. (C) Lysates from BafA1-treated HeLa cells were analyzed by immunoblotting. See also Figure S5.

Figure 5. SLR-specific delivery routes of cargo candidates

(A) Lysates from clonal TOLLIP (#1) and p62 (#1) KOs as well as from parental HeLa cells were analyzed by immunoblotting. (B,C) Homogenates from clonal TOLLIP (B) or p62 (C) KOs as well as parental cells were left untreated or incubated with proteinase K and subjected to immunoblot analysis. (D,E) Quantification of proteinase K protected cargo proteins from (B,C) in parental versus TOLLIP (D) or p62 (C) KO cells. All density values were normalized to GAPDH which was found to be proteinase K indigestible. Data represents mean ± SD. (F,G) BafA1-treated HeLa cells were fixed and stained for TOLLIP or p62 together with CD63 (F) or WIPI2 (G). Scale bars, 10 µm. Insets show single and merged channel magnifications of boxed areas. (H) Electron micrographs of indicated APEX2 fusion expressing HeLa cells treated with BafA1. Upon fixation, cells were incubated with DAB and H_2O_2 followed by standard embedding and ultrathin sectioning. Scale bars, 250 nm. (I) Fixed HeLa cells expressing mCherry-RAB5-Q79L were stained with indicated antibodies and DAPI. Scale bars, 10 µm. Insets show single and merged channel magnifications of boxed areas. (J) Homogenates from mock or mCherry-RAB5-Q79L transfected cells were left untreated or incubated with proteinase K and analyzed by immunoblotting. (K) Quantification of proteinase K protected cargo proteins from (J) in mock versus mCherry-RAB5-Q79L transfected cells. All density values were normalized to GAPDH. Data represents mean ± SD. See also Figure S6, S7 and S8.

Figure 6. Probing molecular requirements for cargo engulfment by SLRs

(A) Immunoblotting of lysates from HeLa cells differentially treated with BafA1 and ATG8-E1 (top) or Btz and Ub-E1 (bottom). (B) Workflow of inhibitor combined autophagosome content profiling. (C) Pearson's correlation of 3 biological replicates. (D) Number of cargo candidates found under basal conditions and ATG8-E1 or Ub-E1 inhibitor treatment in HeLa cells. "Up" and "down" indicate basal cargo candidates with significant increases or decreases, respectively. "New" represents cargo proteins that were absent under basal conditions but significantly increased upon inhibitor treatments. (E,F) Known autophagy components and cargo candidates with significant inhibitor induced changes identified by at least two (E) or only

a single (F) APEX2 bait under basal conditions. (G) GO term enrichment of new cargo proteins with ATG8-E1 or Ub-E1 induced increases. BP, biological process, CC, cellular component, MF, molecular function. (H) Pearson's correlation, total and overlapping proteins of biological triplicates. (I) Pie chart of proteins profiled by APEX2-LC3B in parental and Rec-6-KO HeLa cells. (J) Volcano plot of up-regulated and down-regulated proteins in Rec-6-KO versus parental cells (p-value ≤ 0.05, students *t*-test). (K) APEX2-LC3B profiled proteins that were present in parental but absent in Rec-6-KO cells. Known autophagy components are marked italic. (L) Heat map representation of the SLR dependency of basal LC3B cargo identified in I and J. See also Figure S6 and S8.

Figure 7. Cargo content changes under proteostasis challenging conditions

(A) APEX2-p62 HeLa cells treated with BafA1, Puro or Btz were fixed and stained with indicated antibodies and DAPI. Scale bars, 10 μm. (B) Mock, GFP or GA_{175}-GFP transfected HEK293T cells were grown with BafA1 prior to fixation and immunolabeling. Scale bars, 10 μm. (C) Workflow of autophagosome content profiling upon Btz, Puro or GA_{175} treatment. (D) Pearson's correlation of biological triplicates. (E) Number of cargo candidates found under basal conditions and Btz, Puro or GA_{175} treatment. "Up" and "down" indicate basal cargo candidates with significant increases or decreases, respectively. "New" represents cargo proteins that were absent under basal conditions but significantly increased upon Btz, Puro or GA_{175} treatment. (F) Known machinery and cargo as well as cargo candidates with significant proteotoxicity induced changes. (G) GO term enrichment of new cargo proteins with Btz, Puro or GA_{175} induced increases. BP, biological process, CC, cellular component, MF, molecular function. (H) Working model for differential SLR-mediated autophagy cargo routing. See also Figure S9.

STAR METHODS

RESOURCE AVAILABILITY

Lead Contact

Further information and requests for resources and reagents should be directed to and will be fulfilled by the Lead Contact, Christian Behrends (christian.behrends@mail03.med.uni-muenchen.de).

Materials Availability

All unique reagents generated in this study are available from the Lead Contact with a completed Materials Transfer Agreement.

Data and Code Availability

The accession number for the proteomic dataset reported in this paper is PRIDE: PXD020758 (username: reviewer95184@ebi.ac.uk, password: SshnvPb1). Original data (confocal microscopy images, electron micrographs and immunoblots) have been deposited to Mendeley Data: https://data.mendeley.com/datasets/mwsncvr8rv/draft?a=ebbef9c0-e1d0-4cb0-ab66-902221689db0

EXPERIMENTAL MODEL

HeLa, HEK293T and HeLa Flp-in T-Rex cells were grown in Dulbecco's modified Eagle medium (DMEM Gibco, #61965-026) supplemented with 10% fetal bovine serum (FBS) and 1% sodium pyruvate. Stable cell lines were additionally grown with the respective antibiotics, either puromycin (2 µg/ml Sigma, #P8833) or hygromycin (20 µg/ml Invitrogen, #10687-010) and blasticidin (4 µg/ml Invivogen, #ANT-BL-1).

METHOD DETAILS

Cloning

ORFs flanked with attB sites were cloned into the Gateway entry vector pDONR233. ORFs from the pDONR233 were then introduced into one of the following destination vectors: N-

terminal myc-APEX2 pNEWS (Le Guerroue et al., 2017) or N/C-terminal myc-APEX2 pHAGE vectors (this work).

Cell line generation

For generation of stable inducible HeLa Flp-In cells, pcDNA5/FRT vectors containing the respective myc-AP2-inserts were transfected together with pOG44 (1:9) using Lipofectamine 2000 followed by selection with 20 µg/ml hygromycin and 4 µg/ml blasticidin. Construct expression was induced using doxycycline for 24 h. Lentiviral transfection for the generation of stable HeLa or HEK293T GA_{175}-GFP cells (Zhou et al., 2017) with N-terminal myc-APEX2 pHAGE vectors, was carried out using Lipofectamine 2000 with a ratio of 2:10 (µg DNA / µl Lipofectamine 2000). Cells were then selected by addition of Puromycin (2 µg/ml) 48 h post-transfection. CRISPR / Cas9-mediated genome editing was used to generate TOLLIP and p62 single-knockout cell lines, as well as TOLLIP knockout in the pentaKO cells (Lazarou et al., 2015) using gRNA guides cloned into the pLentiCRISPR-HF1 Puro plasmid (Addgene, #110850) for simultaneous gRNA and Cas9 expression. Three gRNAs were designed for each target using the Broad Institute GPP gRNA designer tool and transfected with Lipofectamine 2000 at a ratio of 1:6 (µg DNA / µl Lipofectamine 2000). Cells were selected with Puromycin (2 µg/ml) 48 h post-transfection and single-cell colonies were obtained by limiting dilution plating in 96-well plates.

Transfections & Treatments

Plasmids were transfected using PEI (Polyethylenimine, Polysciences Europe GmbH) or Lipofectamine 2000 (Invitrogen) according to standard protocols. Reagents were used at the following concentrations for the indicated incubation times: Doxycycline (Sigma, 4 µg/ml, 24 h), BafA1 (Biomol, 200 nM, 2 h), Torin1 (Tocris, 250 nM, 2h), Bortezomib (LC Labs, 1 µM, 8 h), Puromycin (Sigma, 5 µg/ml, 2h), Ub-E1 inhibitor (MLN7243, Takeda, 1 µM, 4 h), ATG8-E1 inhibitor (ML00792183, Takeda, 1 µM, 8 h), SAR405 (medchemexpress, 1 µM, 2 h), MRT68921 (Sigma-Aldrich, 1 µM, 4 h,), GW4869 (Sigma-Aldrich, 5 µM, 24 h), U18886A

(Sigma-Aldrich, 5 µg/ml, 48 h), Biotin-Phenol (IrisBiotech, 500 µM, 30 min), H_2O_2 (Sigma, 1 mM, 1 min), proteinase K (Roche, 30 µg/ml for 30 min or 100 µg/ml for 1 h), *RAPI*Gest™ (Waters, 0.1%, 30 min or 1 h), Triton X-100 (Merck, 0.2%, 30 min), PMSF (Sigma-Aldrich, 10 mM). For RNAi, cells were reverse transfected with Lipofectamine RNAimax (Invitrogen) using ON-Target smart pools (Dharmacon) against ATG14 (L-020438-01-0005), CHMP4B (L-018075-01-0005) or non-targeting control (D-001810-01-20) according to the manufacturer's instructions. Cells were typically harvested 48 h after transfection. For starvation: culturing medium was replaced with EBSS (Sigma, E2888, 4 h) after two washes.

Antibodies

The following primary antibodies were used for immunoblotting (IB) at a concentration of 1:1,000 in 5% milk in TBS-Tween20 (0.5%) and/or for immunofluorescence (IF) at a concentration of 1:500 0.1% BSA-PBS unless stated otherwise: APEX (IgG2A Regina Feederle, custom made, IB 1:200), ATG14 (MBL, M184-3), ATG7 (Cell signaling, 8558, blocked in 5% BSA), ATG9A (Abcam, ab108338), Biotin (Pierce, 31852, IB 1:5,000), ß-Actin (Sigma, A5316, 1:5,000), anti-biotin-FITC (Abcam, ab106219, IF 1:600), CALNEXIN (Abcam, ab22595), CCPG1 (ptglab, 13861-1-AP), CD63 (Abcam, ab59479), CHMP4B (Abcam, ab105767), c-myc (Bethyl, A190-104A), EEA1 (cell signaling, 2411), Flag M2 (Cell Signaling, 2368), G6PD (Abcam, ab993), GAPDH (Thermo Fisher Scientific, AM4300), GIPC1 (Thermo Fisher Scientific, PA5-27161, Abcam, ab5951), GNB2L1 (Abcam, ab62735), HA.11 Clone 16B12 (Covance / Biolegend, MMS-101P901501), HGS (Abcam, ab155539), ITCH (Abcam, ab220637), KBTBD7 (Novus Biologicals, NBP1-92040), KEAP1 (Abcam, ab139729, ab181144), LC3 (Cell Signaling, 2775, blocked in 5% BSA, MBL, PM036, IF 1:300), LEGUMAIN (R&D systems, AF2199, IB in I-block), myc 9E10 (Regina Feederle, custom made, IB 1:100, IF 1:250), NBR1 (AbD Serotec, MCA3240Z, Abcam, ab219862), NDFIP1 (Abcam, ab236892), NDP52 (Abcam, ab68588), OPTN (ptglab, 10837-1-AP, Abcam, ab23666), p62 (BD, 610832, MBL, PM045, BD, 610832), PCNA (Santa Cruz, sc-7907), PDCD6 (Abcam, ab133326), PDCD6IP (Merck, HPA011905-100UL), PRKAR1A (ptglab, 20358-1-AP), RAB5C

(Sigma, HPA003426), RAB7 (Cell Signaling, 2094, Abcam ab50533), RHEB (Abcam, ab92313, Cell Signaling, 13879), RHOA (Cell Signaling, 2117P), SAR1B (Santa Cruz, sc-517425), SCAMP3 (Thermo Fisher Scientific, PA5-67150), SCARB1 (Abcam, ab217318), SLC38A9 (Abcam, ab81687), STAM (ptglab, 12434-1-AP), STIP1 (Abcam, ab126724, IB in I-block), TAX1BP1 (Bethyl, A303-791A-T), TNIP1 (Bethyl, A304-508A-T), TOLLIP (Abcam, ab187198), TRAF2 (Bethyl, A303-461A-T), TUBULIN (Abcam, ab7291), Ubiquitin (clone FK2 Merck, 04-263), UBQLN2 (Cell Signaling, 14653, 85509S IF 1:300), ULK1 (Cell Signaling, 8054), VANGL1 (Abcam, ab242311, Sigma, SAB1408053), VAPA (Sigma, HPA009174), VAPB (Sigma, HPA013144), VCP (Bethyl, A300-588A), WIPI2 (Abcam, ab105459). The following secondary antibodies were used at a concentration of 1:10,000 for IB and 1:1,000 for IF: anti-mouse-HRP (Promega, #W402B), anti-rabbit-HRP (Promega, #W401B), anti-goat-HRP (Promega, V8051), anti-rat-HRP (Sigma, #A-9037), Donkey anti-rb-555 (Life Technologies, A31572), Goat anti-rb-488 (Life Technologies, A11034), Goat anti-mouse-555 (Life Technologies, A21424), Goat anti-mouse-488 (Life Technologies, A11001), Donkey anti-goat-555 (Life Technologies, A21432), Donkey anti-goat-488 (Life Technologies, A11055).

Immunoblotting

Cells were lysed in RIPA-buffer (50 mM Tris, 150 mM NaCl, 0.1% SDS, 0.5% sodium deoxycholate, 1% NP-40, 1x protease inhibitors (Roche) and 1x PhosStop (Roche)). Lysates were cleared by centrifugation at 4°C for 10 min and boiled in sample buffer (200 mM Tris-HCL, 6% SDS, 20% Glycerol, 0.1 g/ml DTT and 0.01 mg Bromophenol Blue). Samples were submitted to SDS-PAGE and transferred to nitrocellulose membranes. Membranes were blocked in 5% milk or 5% BSA in TBS-T (0.1% Tween-20 in TBS) depending on the antibody. Immunoblots were incubated with primary antibodies at 4°C overnight in blocking buffer (1:10 in TBS-T), washed with TBS-T, incubated with secondary HRP-conjugated antibodies for 1 h at room temperature, washed again with TBS-T before analysis by enhanced chemiluminescence.

Immunofluorescence

Cells were grown on coverslips, washed 3x in DPBS (Gibco) and fixed with 4% PFA (Santa Cruz) for 10 min. Cells were then permeabilized with 0.5% Triton X-100 (Merck) for 10 min and blocked in 1% BSA for 1 h at room temperature before sequential staining with primary and secondary antibodies for 1 h each at room temperature in the dark. Coverslips were mounted with Prolong Gold with DAPI (Invitrogen) and imaged after over-night incubation using a Zeiss LSM800 Confocal microscope with an oil-immersion objective at 63x magnification. Images where then processed using the Fiji distribution of the ImageJ software (version 1.8.0).

Proximity labeling

APEX2-mediated biotinylation of cells was carried out as described before (Hung et al., 2016). In brief, cells were supplemented with 500 µM biotin-phenol (IrisBiotech) for 30 min at 37°C before addition of 1 mM H_2O_2 at room temperature. Cells were then first washed with quencher solution (1 mM sodium azide, 10 mM sodium ascorbate and 5 mM Trolox in DPBS), then with DPBS, scraped and harvested.

Proteinase K digest

All steps were carried out at 4°C unless stated otherwise. Cells were washed and suspended in homogenization buffer I (10 mM KCl, 1.5 mM $MgCl_2$, 10 mM HEPES-KOH and 1 mM DTT pH 7.5). After 20 min of incubation in an overhead shaker, cells were dounced with a tight-fitting pestle and mixed with homogenization buffer II (375 mM KCl, 22.5 mM $MgCl_2$, 220 mM HEPES-KOH and 0.5 mM DTT pH 7.5) at a ratio 1:5 (homogenization buffer I:II). Cleared lysates were obtained by centrifugation at 600xg for 10 min. For immunoblotting, 30 µg/ml proteinase K was added for 30 min before inhibition of its activity by PMSF. For the control digestions 0.2% Triton X-100 or 0.1% *RAPI*Gest™ were added in addition to the proteinase K. Samples were then supplemented with sample buffer and submitted to SDS-PAGE. For mass spectrometry, samples were treated with 100 µg/ml Proteinase K for 1 h at 37°C and for control

samples 0.1% *RAPI*Gest™ was additionally added. Digested material was separated from membrane-protected material by centrifugation at 17,000xg for 15 min.

Streptavidin-pulldown

APEX2-labeled pellets after proteinase K digestion or without digestion, to identify cellular interactors, were suspended in RIPA buffer containing quenching components (50 mM Tris, 150 mM NaCl, 0.1% SDS, 0.5% sodium deoxycholate, 1% Triton X-100, 1x protease inhibitors (Roche), 1x PhosStop (Roche), 1 mM sodium azide, 10 mM sodium ascorbate and 1 mM Trolox), briefly sonified and cleared by centrifugation at 10,000xg. Supernatants were then incubated over-night on pre-equilibrated Streptavidin-Agarose (Sigma). Subsequently, the samples were essentially processed as described before (Lobingier et al., 2017). Briefly, samples were washed 3x in RIPA buffer with quenching components and 3x in 3 M Urea buffer (in 50 mM NH_4HCO_3) prior to incubation with TCEP (5 mM final) for 30 min at 55°C and shaking. Samples were alkylated with IAA (10 mM final) for 20 min at room temperature, quenched by addition of DTT (20 mM final) followed by 2 washes with 2 M Urea buffer (in 50 mM NH_4HCO_3) and over-night trypsin digestion with 1 µg trypsin per 20 µl beads at 37°C. Supernatants were collected from the resin plus two additional washes with 2M Urea buffer, acidified with trifluoroacetic acid (1% final) and their volume decreased by vacuum centrifugation. Digested peptides were desalted on custom-made C18 stage tips and reconstituted with 0.5% acetic acid for MS analysis.

Lyso-IP

Lyso-IP was performed similar as described before (Abu-Remaileh et al., 2017). In brief, TMEM192-HA and TMEM192-FLAG cells were grown in the presence of BafA1 (200 nM, 2 h), washed twice in PBS, scraped off and transferred to tubes on ice. All proceeding steps were carried out at 4°C unless stated otherwise and all buffers were supplemented with protease inhibitors. After centrifugation, cells were suspended in LysoIP buffer (50 mM KCl, 100 mM KH_2PO_4 and 100 mM K_2HPO_4 pH 7.2) and dounce homogenized. Nuclei and unbroken cells

were pelleted at 1,500xg for 10 min and the supernatant was transferred to fresh tubes and supplemented with 40 µl pre-equilibrated HA-magnetic beads (ThermoFisher). After 1 h rotating incubation, the beads were washed 3x in salt buffer (LysoIP buffer with 300 mM NaCl) and eluted by suspension of the beads in 150 µl Urea buffer (8M Urea, 50 mM Tris pH8, 150 mM NaCl) followed by 30 min rotating incubation. The eluate was sonicated for 5 min and sequentially treated with 5 mM DTT (Sigma, 30 min, 55°C and shaking), 15 mM IAA (Sigma, 30 min, room temperature) and 10 mM DTT (15 min at room temperature). Proteins were precipitated by adding 600 µl methanol (Roth) and 150 µl chloroform (Merck), vortexing and adding 450 µl of MS-grade H_2O (Roth) and vortexing again. After centrifugation at 14,000xg for 5 min, the hydrophilic phase was removed. 450 µl methanol were added and again spun down at 14,000xg for 5 min. Samples were completely dried by vacuum centrifugation at 30°C and proteins were suspended in 30 µl 50 mM ABC buffer followed by digestion with 1 µg trypsin overnight at 37°C. Digestion was stopped by adding 30 µl 50% acetonitrile (Roth) / 5% formic acid (Merck) and incubated for 10 min. Subsequently, all liquids were evaporated by vacuum centrifugation. Peptides were suspended in 30 µl 5% acetonitrile / 1% TFA (Honeywell Fluka), desalted on custom-made C18 stage-tips and reconstituted for MS analysis as described above.

Electron Microscopy

HeLa cells expressing APEX2 fusions were grown on aclar sheets (Science Services) and induced by Doxycycline 24 h before fixation. Cells were supplemented with 4.83 µM Hemin chloride (ROTH) for 16 h and treated with 200 nM BafA1 (Biomol) 2 h before fixation. Cells were fixed in 2.5% glutaraldehyde (EM-grade, Science Services) in 0.1 M sodium cacodylate buffer (pH 7.4, CB) for 30 min. Fixation and the following processing steps were carried out on ice. After washes in CB, endogenous peroxidases were blocked in 20 mM glycine (Sigma) in CB for 5 min and cells washed in CB. 1x diaminobenzidine (DAB) in CB with 2 mM calcium chloride was prepared from a 10x DAB stock (Sigma) in hydrochloric acid (Sigma) and added to the cells for 5 min without and for another 40 min with 10 mM H_2O_2 (Sigma). After washes

in CB, cells were postfixed in reduced osmium (1.15% osmium tetroxide, Science Services, 1.5% potassium ferricyanide, Sigma) for 30 min, washed in CB and water and incubated overnight in 0.5% aqueous uranylacetate (ScienceServices). Dehydration was accomplished using a graded series of ice-cold ethanol. Cell monolayers were infiltrated in epon (Serva) and cured for 48 h at 60°C. Cells were ultrathin sectioned at 50 nm on formvar-coated copper grids (Plano). TEM images were acquired on a JEM 1400plus (JEOL) using the TEMCenter and Shotmeister software packages (JEOL) and analyzed in ImageJ.

QUANTIFICATION AND STATISTICAL ANALYSIS

MS data collection and analysis

Samples were loaded onto 75 µm x 15 cm fused silica capillaries (custom-made) packed with C18AQ resin (Reprosil-Pur 120, 1.9 µm, Dr. Maisch HPLC) using an Easy-nLC1200 liquid chromatography. Peptide mixtures were separated at a 400 nl/min flow rate using a 35 min ACN gradient in 0.5% acetic acid (5–38% ACN gradient for 23 min followed by 38-60% ACN gradient for 3 min and 60-95% ACN gradient for 2 min plus another 3 min at 95% CAN prior to 95-5% gradient for 2 min and another 2 min at 5% ACN) and detected on an Q Exactive HF mass spectrometer (Thermo Scientific). Dynamic exclusion was enabled for 20 s and singly charged species, charge states above 8 or species for which a charge could not be assigned were rejected. MS raw data was analyzed using MaxQuant (version 1.6.0.1) (Cox and Mann, 2008) and a human Uniprot FASTA reference proteome (UP000005640) in reverted decoy mode with the following allowance: methionine oxidation and protein N-terminus acetylation as variable modifications, cysteine carbamidomethylation as fixed modifications, 2 missed cleavages and 5 modifications per peptide, minimum peptide length of 7 amino acids, first search peptide tolerance of ±20 ppm, main search peptide tolerance of ±4.5, match between runs, label-free quantification (LFQ), as well as protein, peptide and site level false discovery rates of 0.01. For further processing, MaxQuant output files (proteingroups) were loaded into Perseus (version 1.6.5.0) (Tyanova et al., 2016) where matches to common contaminants, reverse identifications, identifications based only on site-specific modifications and with less

than 2 peptides and MS/MS counts were removed. For proteinase K treated APEX2 bait samples, identifications from the *RAPI*Gest^{TM} and proteinase K treated controls were subtracted. Only proteins with LFQ intensities in 2 out of 3 biological replicates in at least one experimental group were kept for the subsequent label-free quantification. LFQ intensities were log_2 transformed and missing values were replaced with random numbers drawn from a normal distribution. Student *t*-tests were used to determine the statistical significance of the abundance alterations of proteins identified in the proximity of APEX2 baits or in immuno-isolated lysosomes between experimental conditions. TMEM106B vesicle content candidates were defined by p-values ≤ 0.05 and T-test differences ≥ 2 between TMEM106B DMSO or BafA1/Torin1 versus HeLa. Basal cargo candidates were defined by p-values ≤ 0.05 and *t*-test differences > 0 between BafA1 versus DMSO treated APEX2 bait samples. Inhibitor (ATG8-E1, Ub-E1, Btz and Puro) and polyGA sensitive cargoes were classified by p-values ≤ 0.05 between with or without inhibitor or GA_{175}-GFP versus GFP treated APEX2 baits with BafA1. Proximity partners were defined by T-test differences ≥ 1 between BafA1 and DMSO treated APEX2 bait samples versus three background controls (empty parental HeLa and APEX2-LC3B DMSO or BafA1 without biotin-phenol). In addition, significantly altered proteins from the BafA1 versus DMSO comparison of APEX2-LC3B without biotin-phenol were excluded, while all proteins with p-values ≤ 0.05 in one of the 4 comparisons of APEX2 baits versus the background controls and in the BafA1 versus DMSO comparison of APEX2 baits were retained as candidates. Out of this combined pool of proximity partners only proteins with *t*-test differences ≥ 0.5 or ≤ -0.5 in the BafA1 versus DMSO comparison of APEX2 baits were classified as up- or downregulated upon BafA1 treatment. For LysoIP, proteins with p-values ≤ 0.05 and *t*-test differences ≥ 0.5 in the comparison of parental TMEM192-HA versus parental empty were defined as lysosomal (luminal, TM or PM) candidates. Furthermore, candidates with p-values ≤ 0.05 and *t*-test differences ≤ -0.2 in the comparison of Rec-6-KO or ATG8-6-KO versus parental TMEM192-HA but not in the comparison of Rec-6-KO or ATG8-6-KO TMEM192-FLAG versus parental TMEM192-FLAG were assigned for the autophagy-

sensitive lyso-proteome. Annotation enrichment and interactome analysis was performed using DAVID (Huang et al., 2007) and BioGRID (Stark et al., 2006), respectively.

Immunoblot and immunofluorescence quantification

Quantification and statistical analyses of 3 independent immunoblots or 3 independent images were performed using ImageJ (version 1.8.0) and Python (version 3.7.6). Data represents mean ± SD. Statistical significance was calculated with unpaired Student's *t*-test. p-values ≤ 0.05 were considered significant (p-value ≤ 0.05 = *, ≤ 0.01 = ** and ≤ 0.001 = ***). Pixel intensity analysis of line graphs was performed using Zenblue (version 2.5) and Pearson's correlation coefficient (*R*) was determined in Excel.

Table S1. Summary of proximity and organellar proteomics data. Related to Figure 2, 3, 6, 7, S2, S3, S4, S8 and S9. Contains lists and statistical analysis of autophagy cargo candidates, proximity partners, endosomal and lysosomal proteins as well as proteinase K resistant background contaminants identified by mass spectrometry.

References

Abu-Remaileh, M., Wyant, G. A., Kim, C., Laqtom, N. N., Abbasi, M., Chan, S. H., Freinkman, E., & Sabatini, D. M. (2017). Lysosomal metabolomics reveals V-ATPase- and mTOR-dependent regulation of amino acid efflux from lysosomes. *Science, 358*(6364), 807-813.

Birgisdottir, A. B., Lamark, T., & Johansen, T. (2013). The LIR motif - crucial for selective autophagy. *J Cell Sci, 126*(Pt 15), 3237-3247.

Cox, J., & Mann, M. (2008). MaxQuant enables high peptide identification rates, individualized p.p.b.-range mass accuracies and proteome-wide protein quantification. *Nat Biotechnol, 26*(12), 1367-1372.

Deosaran, E., Larsen, K. B., Hua, R., Sargent, G., Wang, Y., Kim, S., Lamark, T., Jauregui, M., Law, K., Lippincott-Schwartz, J., et al. (2013). NBR1 acts as an autophagy receptor for peroxisomes. *J Cell Sci, 126*(Pt 4), 939-952.

Deretic, V. (2012). Autophagy as an innate immunity paradigm: expanding the scope and repertoire of pattern recognition receptors. *Curr Opin Immunol, 24*(1), 21-31.

Fu, T., Liu, J., Wang, Y., Xie, X., Hu, S., & Pan, L. (2018). Mechanistic insights into the interactions of NAP1 with the SKICH domains of NDP52 and TAX1BP1. *Proc Natl Acad Sci U S A, 115*(50), E11651-E11660.

Genau, H. M., Huber, J., Baschieri, F., Akutsu, M., Dotsch, V., Farhan, H., Rogov, V., & Behrends, C. (2015). CUL3-KBTBD6/KBTBD7 ubiquitin ligase cooperates with GABARAP proteins to spatially restrict TIAM1-RAC1 signaling. *Mol Cell, 57*(6), 995-1010.

Guo, Q., Lehmer, C., Martinez-Sanchez, A., Rudack, T., Beck, F., Hartmann, H., Perez-Berlanga, M., Frottin, F., Hipp, M. S., Hartl, F. U., et al. (2018). In Situ Structure of Neuronal C9orf72 Poly-GA Aggregates Reveals Proteasome Recruitment. *Cell, 172*(4), 696-705 e612.

Heo, J. M., Harper, N. J., Paulo, J. A., Li, M., Xu, Q., Coughlin, M., Elledge, S. J., & Harper, J. W. (2019). Integrated proteogenetic analysis reveals the landscape of a mitochondrial-autophagosome synapse during PARK2-dependent mitophagy. *Sci Adv, 5*(11), eaay4624.

Heo, J. M., Ordureau, A., Paulo, J. A., Rinehart, J., & Harper, J. W. (2015). The PINK1-PARKIN Mitochondrial Ubiquitylation Pathway Drives a Program of OPTN/NDP52 Recruitment and TBK1 Activation to Promote Mitophagy. *Mol Cell, 60*(1), 7-20.

Hipp, M. S., Kasturi, P., & Hartl, F. U. (2019). The proteostasis network and its decline in ageing. *Nat Rev Mol Cell Biol, 20*(7), 421-435.

Huang, D. W., Sherman, B. T., Tan, Q., Kir, J., Liu, D., Bryant, D., Guo, Y., Stephens, R., Baseler, M. W., Lane, H. C., et al. (2007). DAVID Bioinformatics Resources: expanded annotation database and novel algorithms to better extract biology from large gene lists. *Nucleic Acids Res, 35*(Web Server issue), W169-175.

Hung, V., Udeshi, N. D., Lam, S. S., Loh, K. H., Cox, K. J., Pedram, K., Carr, S. A., & Ting, A. Y. (2016). Spatially resolved proteomic mapping in living cells with the engineered peroxidase APEX2. *Nat Protoc, 11*(3), 456-475.

Hyer, M. L., Milhollen, M. A., Ciavarri, J., Fleming, P., Traore, T., Sappal, D., Huck, J., Shi, J., Gavin, J., Brownell, J., et al. (2018). A small-molecule inhibitor of the ubiquitin activating enzyme for cancer treatment. *Nat Med, 24*(2), 186-193.

Jain, A., Lamark, T., Sjottem, E., Larsen, K. B., Awuh, J. A., Overvatn, A., McMahon, M., Hayes, J. D., & Johansen, T. (2010). p62/SQSTM1 is a target gene for transcription factor NRF2 and creates a positive feedback loop by inducing antioxidant response element-driven gene transcription. *J Biol Chem, 285*(29), 22576-22591.

Jongsma, M. L., Berlin, I., Wijdeven, R. H., Janssen, L., Janssen, G. M., Garstka, M. A., Janssen, H., Mensink, M., van Veelen, P. A., Spaapen, R. M., et al. (2016). An ER-Associated Pathway Defines Endosomal Architecture for Controlled Cargo Transport. *Cell, 166*(1), 152-166.

Katoh, Y., Shiba, Y., Mitsuhashi, H., Yanagida, Y., Takatsu, H., & Nakayama, K. (2004). Tollip and Tom1 form a complex and recruit ubiquitin-conjugated proteins onto early endosomes. *J Biol Chem, 279*(23), 24435-24443.

Kim, P. K., Hailey, D. W., Mullen, R. T., & Lippincott-Schwartz, J. (2008). Ubiquitin signals autophagic degradation of cytosolic proteins and peroxisomes. *Proc Natl Acad Sci U S A, 105*(52), 20567-20574.

Kirkin, V., Lamark, T., Sou, Y. S., Bjorkoy, G., Nunn, J. L., Bruun, J. A., Shvets, E., McEwan, D. G., Clausen, T. H., Wild, P., et al. (2009a). A role for NBR1 in autophagosomal degradation of ubiquitinated substrates. *Mol Cell, 33*(4), 505-516.

Kirkin, V., McEwan, D. G., Novak, I., & Dikic, I. (2009b). A role for ubiquitin in selective autophagy. *Mol Cell, 34*(3), 259-269.

Komatsu, M., Kurokawa, H., Waguri, S., Taguchi, K., Kobayashi, A., Ichimura, Y., Sou, Y. S., Ueno, I., Sakamoto, A., Tong, K. I., et al. (2010). The selective autophagy substrate p62 activates the stress responsive transcription factor Nrf2 through inactivation of Keap1. *Nat Cell Biol, 12*(3), 213-223.

Korac, J., Schaeffer, V., Kovacevic, I., Clement, A. M., Jungblut, B., Behl, C., Terzic, J., & Dikic, I. (2013). Ubiquitin-independent function of optineurin in autophagic clearance of protein aggregates. *J Cell Sci, 126*(Pt 2), 580-592.

Lamark, T., Perander, M., Outzen, H., Kristiansen, K., Overvatn, A., Michaelsen, E., Bjorkoy, G., & Johansen, T. (2003). Interaction codes within the family of mammalian Phox and Bem1p domain-containing proteins. *J Biol Chem, 278*(36), 34568-34581.

Langemeyer, L., Frohlich, F., & Ungermann, C. (2018). Rab GTPase Function in Endosome and Lysosome Biogenesis. *Trends Cell Biol, 28*(11), 957-970.

Lazarou, M., Sliter, D. A., Kane, L. A., Sarraf, S. A., Wang, C., Burman, J. L., Sideris, D. P., Fogel, A. I., & Youle, R. J. (2015). The ubiquitin kinase PINK1 recruits autophagy receptors to induce mitophagy. *Nature, 524*(7565), 309-314.

Le Guerroue, F., Eck, F., Jung, J., Starzetz, T., Mittelbronn, M., Kaulich, M., & Behrends, C. (2017). Autophagosomal Content Profiling Reveals an LC3C-Dependent Piecemeal Mitophagy Pathway. *Mol Cell, 68*(4), 786-796 e786.

Leidal, A. M., Huang, H. H., Marsh, T., Solvik, T., Zhang, D., Ye, J., Kai, F., Goldsmith, J., Liu, J. Y., Huang, Y. H., et al. (2020). The LC3-conjugation machinery specifies the loading of RNA-binding proteins into extracellular vesicles. *Nat Cell Biol, 22*(2), 187-199.

Lobingier, B. T., Huttenhain, R., Eichel, K., Miller, K. B., Ting, A. Y., von Zastrow, M., & Krogan, N. J. (2017). An Approach to Spatiotemporally Resolve Protein Interaction Networks in Living Cells. *Cell, 169*(2), 350-360 e312.

Lu, K., Psakhye, I., & Jentsch, S. (2014). Autophagic clearance of polyQ proteins mediated by ubiquitin-Atg8 adaptors of the conserved CUET protein family. *Cell, 158*(3), 549-563.

Maejima, I., Takahashi, A., Omori, H., Kimura, T., Takabatake, Y., Saitoh, T., Yamamoto, A., Hamasaki, M., Noda, T., Isaka, Y., et al. (2013). Autophagy sequesters damaged lysosomes to control lysosomal biogenesis and kidney injury. *EMBO J, 32*(17), 2336-2347.

Mancias, J. D., Wang, X., Gygi, S. P., Harper, J. W., & Kimmelman, A. C. (2014). Quantitative proteomics identifies NCOA4 as the cargo receptor mediating ferritinophagy. *Nature, 509*(7498), 105-109.

Mejlvang, J., Olsvik, H., Svenning, S., Bruun, J. A., Abudu, Y. P., Larsen, K. B., Brech, A., Hansen, T. E., Brenne, H., Hansen, T., et al. (2018). Starvation induces rapid degradation of selective autophagy receptors by endosomal microautophagy. *J Cell Biol, 217*(10), 3640-3655.

Mizushima, N., & Komatsu, M. (2011). Autophagy: renovation of cells and tissues. *Cell, 147*(4), 728-741.

Mizushima, N., Yoshimori, T., & Ohsumi, Y. (2011). The role of Atg proteins in autophagosome formation. *Annu Rev Cell Dev Biol, 27*, 107-132.

Mori, K., Weng, S. M., Arzberger, T., May, S., Rentzsch, K., Kremmer, E., Schmid, B., Kretzschmar, H. A., Cruts, M., Van Broeckhoven, C., et al. (2013). The C9orf72 GGGGCC repeat is translated into aggregating dipeptide-repeat proteins in FTLD/ALS. *Science, 339*(6125), 1335-1338.

Nguyen, T. N., Padman, B. S., Usher, J., Oorschot, V., Ramm, G., & Lazarou, M. (2016). Atg8 family LC3/GABARAP proteins are crucial for autophagosome-lysosome fusion but not autophagosome formation during PINK1/Parkin mitophagy and starvation. *J Cell Biol, 215*(6), 857-874.

Nishitoh, H., Kadowaki, H., Nagai, A., Maruyama, T., Yokota, T., Fukutomi, H., Noguchi, T., Matsuzawa, A., Takeda, K., & Ichijo, H. (2008). ALS-linked mutant SOD1 induces ER stress- and ASK1-dependent motor neuron death by targeting Derlin-1. *Genes Dev, 22*(11), 1451-1464.

Nthiga, T. M., Kumar Shrestha, B., Sjottem, E., Bruun, J. A., Bowitz Larsen, K., Bhujabal, Z., Lamark, T., & Johansen, T. (2020). CALCOCO1 acts with VAMP-associated proteins to mediate ER-phagy. *EMBO J*, e2019103649.

Oku, M., & Sakai, Y. (2018). Three Distinct Types of Microautophagy Based on Membrane Dynamics and Molecular Machineries. *Bioessays, 40*(6), e1800008.

Pankiv, S., Clausen, T. H., Lamark, T., Brech, A., Bruun, J. A., Outzen, H., Overvatn, A., Bjorkoy, G., & Johansen, T. (2007). p62/SQSTM1 binds directly to Atg8/LC3 to facilitate degradation of ubiquitinated protein aggregates by autophagy. *J Biol Chem, 282*(33), 24131-24145.

Petherick, K. J., Conway, O. J., Mpamhanga, C., Osborne, S. A., Kamal, A., Saxty, B., & Ganley, I. G. (2015). Pharmacological inhibition of ULK1 kinase blocks mammalian target of rapamycin (mTOR)-dependent autophagy. *J Biol Chem, 290*(18), 11376-11383.

Princely Abudu, Y., Pankiv, S., Mathai, B. J., Hakon Lystad, A., Bindesboll, C., Brenne, H. B., Yoke Wui Ng, M., Thiede, B., Yamamoto, A., Mutugi Nthiga, T., et al. (2019).

NIPSNAP1 and NIPSNAP2 Act as "Eat Me" Signals for Mitophagy. *Dev Cell, 49*(4), 509-525 e512.
Rogov, V., Dotsch, V., Johansen, T., & Kirkin, V. (2014). Interactions between autophagy receptors and ubiquitin-like proteins form the molecular basis for selective autophagy. *Mol Cell, 53*(2), 167-178.
Ronan, B., Flamand, O., Vescovi, L., Dureuil, C., Durand, L., Fassy, F., Bachelot, M. F., Lamberton, A., Mathieu, M., Bertrand, T., et al. (2014). A highly potent and selective Vps34 inhibitor alters vesicle trafficking and autophagy. *Nat Chem Biol, 10*(12), 1013-1019.
Ryan, T. A., Phillips, E. O., Collier, C. L., Jb Robinson, A., Routledge, D., Wood, R. E., Assar, E. A., & Tumbarello, D. A. (2020). Tollip coordinates Parkin-dependent trafficking of mitochondrial-derived vesicles. *EMBO J, 39*(11), e102539.
Sahu, R., Kaushik, S., Clement, C. C., Cannizzo, E. S., Scharf, B., Follenzi, A., Potolicchio, I., Nieves, E., Cuervo, A. M., & Santambrogio, L. (2011). Microautophagy of cytosolic proteins by late endosomes. *Dev Cell, 20*(1), 131-139.
Sarraf, S. A., Shah, H. V., Kanfer, G., Pickrell, A. M., Holtzclaw, L. A., Ward, M. E., & Youle, R. J. (2020). Loss of TAX1BP1-Directed Autophagy Results in Protein Aggregate Accumulation in the Brain. *Mol Cell, 80*(5), 779-795 e710.
Stark, C., Breitkreutz, B. J., Reguly, T., Boucher, L., Breitkreutz, A., & Tyers, M. (2006). BioGRID: a general repository for interaction datasets. *Nucleic Acids Res, 34*(Database issue), D535-539.
Stenmark, H., Parton, R. G., Steele-Mortimer, O., Lutcke, A., Gruenberg, J., & Zerial, M. (1994). Inhibition of rab5 GTPase activity stimulates membrane fusion in endocytosis. *EMBO J, 13*(6), 1287-1296.
Stolz, A., Ernst, A., & Dikic, I. (2014). Cargo recognition and trafficking in selective autophagy. *Nat Cell Biol, 16*(6), 495-501.
Tyanova, S., Temu, T., Sinitcyn, P., Carlson, A., Hein, M. Y., Geiger, T., Mann, M., & Cox, J. (2016). The Perseus computational platform for comprehensive analysis of (prote)omics data. *Nat Methods, 13*(9), 731-740.
von Muhlinen, N., Akutsu, M., Ravenhill, B. J., Foeglein, A., Bloor, S., Rutherford, T. J., Freund, S. M., Komander, D., & Randow, F. (2012). LC3C, bound selectively by a noncanonical LIR motif in NDP52, is required for antibacterial autophagy. *Mol Cell, 48*(3), 329-342.
Wild, P., Farhan, H., McEwan, D. G., Wagner, S., Rogov, V. V., Brady, N. R., Richter, B., Korac, J., Waidmann, O., Choudhary, C., et al. (2011). Phosphorylation of the autophagy receptor optineurin restricts Salmonella growth. *Science, 333*(6039), 228-233.
Xiao, S., Brannon, M. K., Zhao, X., Fread, K. I., Ellena, J. F., Bushweller, J. H., Finkielstein, C. V., Armstrong, G. S., & Capelluto, D. G. S. (2015). Tom1 Modulates Binding of Tollip to Phosphatidylinositol 3-Phosphate via a Coupled Folding and Binding Mechanism. *Structure, 23*(10), 1910-1920.
Yamakami, M., Yoshimori, T., & Yokosawa, H. (2003). Tom1, a VHS domain-containing protein, interacts with tollip, ubiquitin, and clathrin. *J Biol Chem, 278*(52), 52865-52872.
Zhou, Q., Lehmer, C., Michaelsen, M., Mori, K., Alterauge, D., Baumjohann, D., Schludi, M. H., Greiling, J., Farny, D., Flatley, A., et al. (2017). Antibodies inhibit transmission and aggregation of C9orf72 poly-GA dipeptide repeat proteins. *EMBO Mol Med, 9*(5), 687-702.

Figure 1

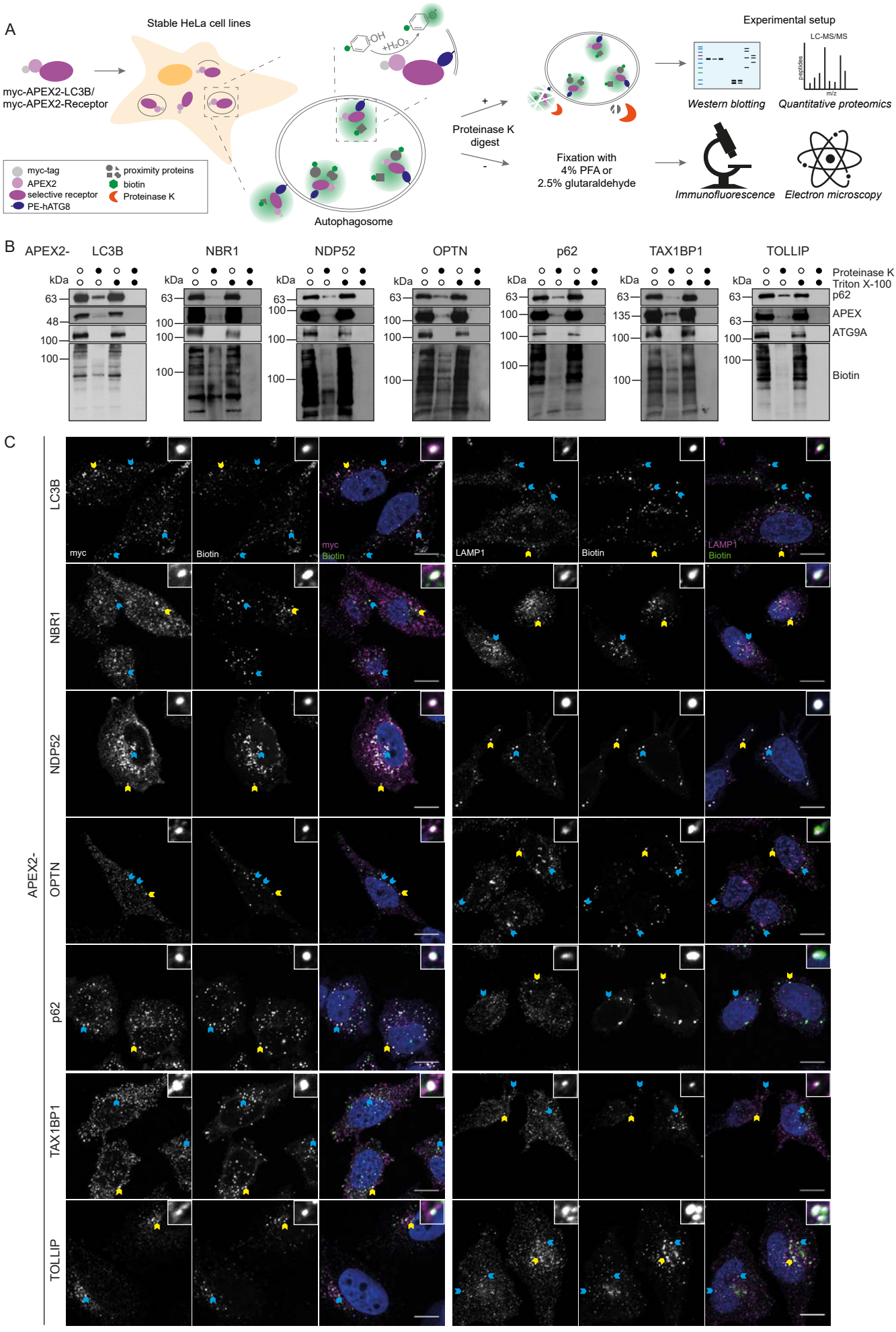
A
Stable HeLa cell lines
myc-APEX2-LC3B/
myc-APEX2-Receptor
myc-tag
APEX2
selective receptor
PE-hATG8
proximity proteins
biotin
Proteinase K
Autophagosome
+H2O2
Proteinase K
digest
Fixation with
4% PFA or
2.5% glutaraldehyde
Experimental setup
LC-MS/MS
Western blotting
Quantitative proteomics
Immunofluorescence
Electron microscopy
B
APEX2-
LC3B
NBR1
NDP52
OPTN
p62
TAX1BP1
TOLLIP
kDa
Proteinase K
Triton X-100
p62
APEX
ATG9A
Biotin
C
APEX2-
LC3B
NBR1
NDP52
OPTN
p62
TAX1BP1
TOLLIP
myc
Biotin
myc
Biotin
LAMP1
Biotin
LAMP1
Biotin

Figure 2

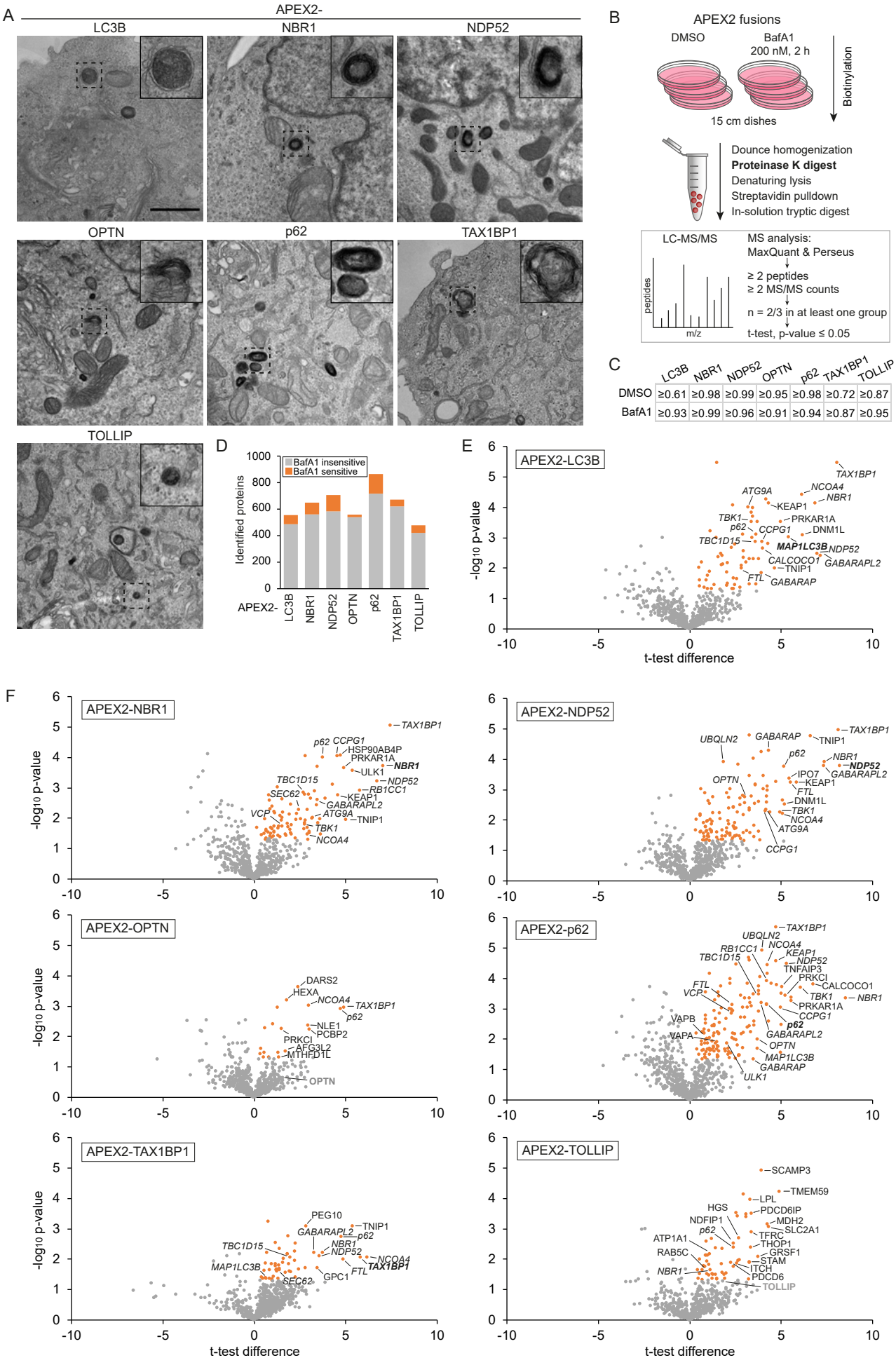
A
APEX2-
LC3B
NBR1
NDP52
OPTN
p62
TAX1BP1
TOLLIP
B
APEX2 fusions
DMSO
BafA1
200 nM, 2 h
Biotinylation
15 cm dishes
Dounce homogenization
Proteinase K digest
Denaturing lysis
Streptavidin pulldown
In-solution tryptic digest
LC-MS/MS
MS analysis:
MaxQuant & Perseus
≥ 2 peptides
≥ 2 MS/MS counts
n = 2/3 in at least one group
t-test, p-value ≤ 0.05
peptides
m/z
C
LC3B NBR1 NDP52 OPTN p62 TAX1BP1 TOLLIP
DMSO ≥0.61 ≥0.98 ≥0.99 ≥0.95 ≥0.98 ≥0.72 ≥0.87
BafA1 ≥0.93 ≥0.99 ≥0.96 ≥0.91 ≥0.94 ≥0.87 ≥0.95
D
BafA1 insensitive
BafA1 sensitive
Identified proteins
APEX2-
E
APEX2-LC3B
-log10 p-value
t-test difference
F
APEX2-NBR1
APEX2-NDP52
APEX2-OPTN
APEX2-p62
APEX2-TAX1BP1
APEX2-TOLLIP

Figure 3

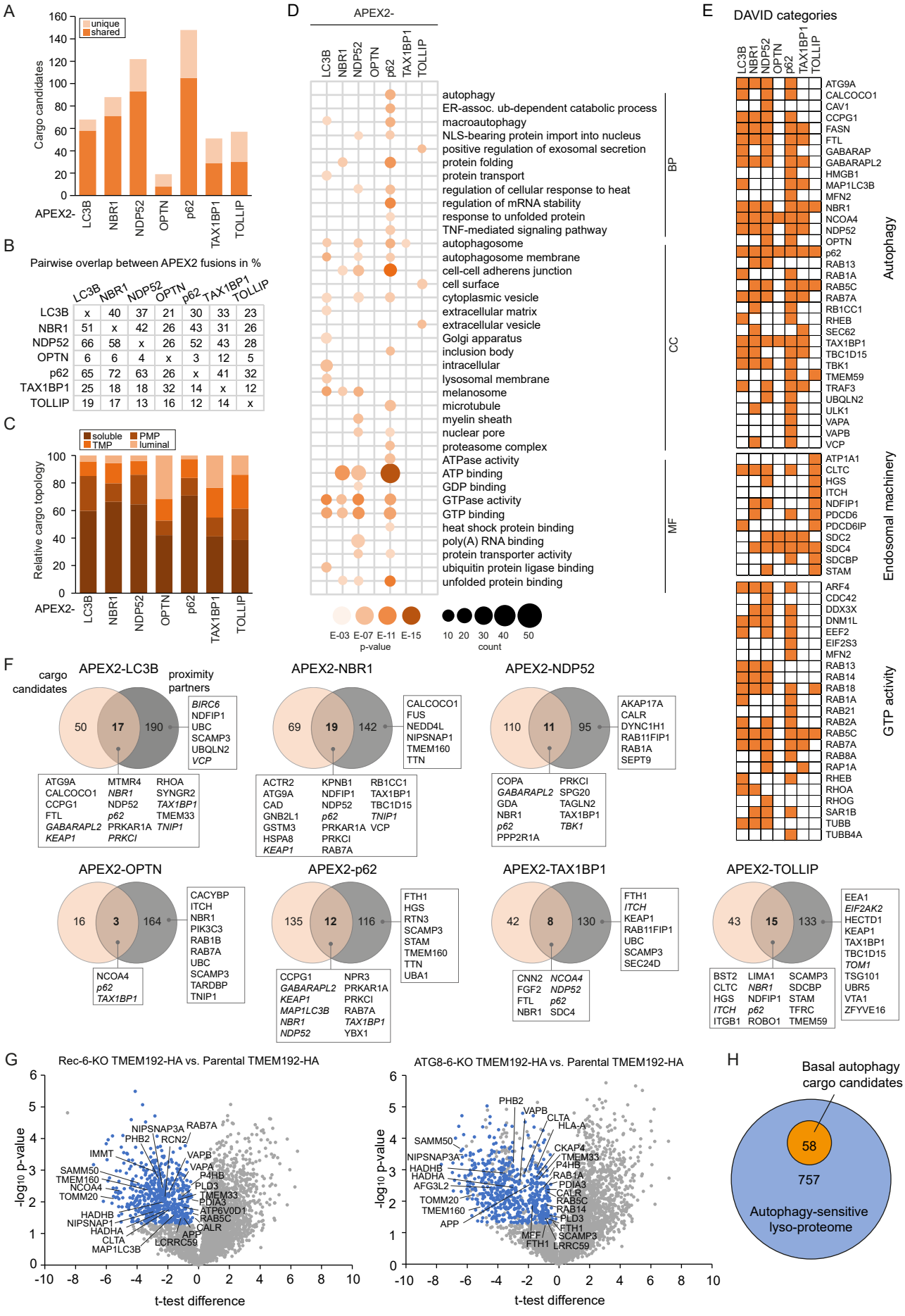
A
unique
shared
Cargo candidates
APEX2-
LC3B
NBR1
NDP52
OPTN
p62
TAX1BP1
TOLLIP
B
Pairwise overlap between APEX2 fusions in %
C
soluble
TMP
PMP
luminal
Relative cargo topology
D
APEX2-
autophagy
ER-assoc. ub-dependent catabolic process
macroautophagy
NLS-bearing protein import into nucleus
positive regulation of exosomal secretion
protein folding
protein transport
regulation of cellular response to heat
regulation of mRNA stability
response to unfolded protein
TNF-mediated signaling pathway
autophagosome
autophagosome membrane
cell-cell adherens junction
cell surface
cytoplasmic vesicle
extracellular matrix
extracellular vesicle
Golgi apparatus
inclusion body
intracellular
lysosomal membrane
melanosome
microtubule
myelin sheath
nuclear pore
proteasome complex
ATPase activity
ATP binding
GDP binding
GTPase activity
GTP binding
heat shock protein binding
poly(A) RNA binding
protein transporter activity
ubiquitin protein ligase binding
unfolded protein binding
BP
CC
MF
E-03 E-07 E-11 E-15
p-value
10 20 30 40 50
count
E
DAVID categories
ATG9A
CALCOCO1
CAV1
CCPG1
FASN
FTL
GABARAP
GABARAPL2
HMGB1
MAP1LC3B
MFN2
NBR1
NCOA4
NDP52
OPTN
p62
RAB13
RAB1A
RAB5C
RAB7A
RB1CC1
RHEB
SEC62
TAX1BP1
TBC1D15
TBK1
TMEM59
TRAF3
UBQLN2
ULK1
VAPA
VAPB
VCP
Autophagy
ATP1A1
CLTC
HGS
ITCH
NDFIP1
PDCD6
PDCD6IP
SDC2
SDC4
SDCBP
STAM
Endosomal machinery
ARF4
CDC42
DDX3X
DNM1L
EEF2
EIF2S3
MFN2
RAB13
RAB14
RAB18
RAB1A
RAB21
RAB2A
RAB5C
RAB7A
RAB8A
RAP1A
RHEB
RHOA
RHOG
SAR1B
TUBB
TUBB4A
GTP activity
F
cargo candidates
proximity partners
APEX2-LC3B
50 17 190
BIRC6
NDFIP1
UBC
SCAMP3
UBQLN2
VCP
ATG9A
CALCOCO1
CCPG1
FTL
GABARAPL2
KEAP1
MTMR4
NBR1
NDP52
TAX1BP1
p62
PRKAR1A
PRKCI
RHOA
SYNGR2
TAX1BP1
TMEM33
TNIP1
APEX2-NBR1
69 19 142
CALCOCO1
FUS
NEDD4L
NIPSNAP1
TMEM160
TTN
ACTR2
ATG9A
CAD
GNB2L1
GSTM3
HSPA8
KEAP1
KPNB1
NDFIP1
NDP52
p62
PRKAR1A
PRKCI
RAB7A
RB1CC1
TAX1BP1
TBC1D15
TNIP1
VCP
APEX2-NDP52
110 11 95
AKAP17A
CALR
DYNC1H1
RAB11FIP1
RAB1A
SEPT9
COPA
GABARAPL2
GDA
NBR1
p62
PPP2R1A
PRKCI
SPG20
TAGLN2
TAX1BP1
TBK1
APEX2-OPTN
16 3 164
CACYBP
ITCH
NBR1
PIK3C3
RAB1B
RAB7A
UBC
SCAMP3
TARDBP
TNIP1
NCOA4
p62
TAX1BP1
APEX2-p62
135 12 116
FTH1
HGS
RTN3
SCAMP3
STAM
TMEM160
TTN
UBA1
CCPG1
GABARAPL2
KEAP1
MAP1LC3B
NBR1
NDP52
NPR3
PRKAR1A
PRKCI
RAB7A
TAX1BP1
YBX1
APEX2-TAX1BP1
42 8 130
FTH1
ITCH
KEAP1
RAB11FIP1
UBC
SCAMP3
SEC24D
CNN2
FGF2
FTL
NBR1
NCOA4
NDP52
p62
SDC4
APEX2-TOLLIP
43 15 133
EEA1
EIF2AK2
HECTD1
KEAP1
TAX1BP1
TBC1D15
TOM1
TSG101
UBR5
VTA1
ZFYVE16
BST2
CLTC
HGS
ITCH
ITGB1
LIMA1
NBRI
NDFIP1
p62
ROBO1
SCAMP3
SDCBP
STAM
TFRC
TMEM59
G
Rec-6-KO TMEM192-HA vs. Parental TMEM192-HA
-log10 p-value
t-test difference
NIPSNAP3A
RAB7A
PHB2
RCN2
IMMT
VAPB
VAPA
SAMM50
P4HB
TMEM160
PLD3
NCOA4
TMEM33
TOMM20
PDIA3
ATP6V0D1
HADHB
RAB5C
NIPSNAP1
CALR
HADHA
APP
CLTA
LCRRC59
MAP1LC3B
ATG8-6-KO TMEM192-HA vs. Parental TMEM192-HA
PHB2
VAPB
CLTA
HLA-A
SAMM50
CKAP4
NIPSNAP3A
TMEM33
HADHB
P4HB
HADHA
RAB1A
AFG3L2
PDIA3
CALR
TOMM20
RAB5C
TMEM160
RAB14
APP
PLD3
FTH1
MFF
SCAMP3
FTH1
LRRC59
H
Basal autophagy cargo candidates
58
757
Autophagy-sensitive lyso-proteome

Figure 4

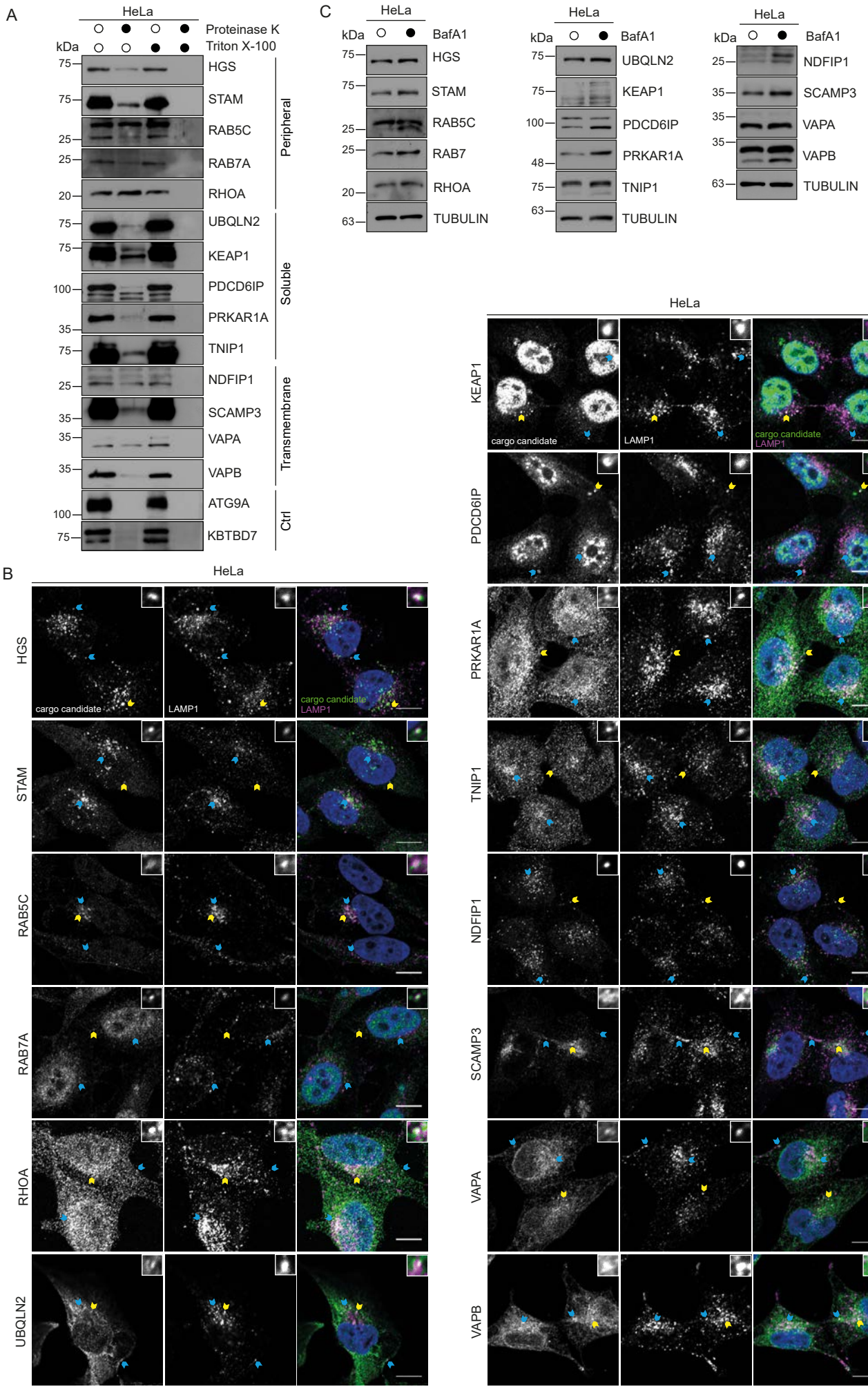
A
HeLa
Proteinase K
Triton X-100
kDa
HGS
STAM
RAB5C
RAB7A
RHOA
UBQLN2
KEAP1
PDCD6IP
PRKAR1A
TNIP1
NDFIP1
SCAMP3
VAPA
VAPB
ATG9A
KBTBD7
Peripheral
Soluble
Transmembrane
Ctrl
C
HeLa
BafA1
kDa
HGS
STAM
RAB5C
RAB7
RHOA
TUBULIN
UBQLN2
KEAP1
PDCD6IP
PRKAR1A
TNIP1
TUBULIN
NDFIP1
SCAMP3
VAPA
VAPB
TUBULIN
B
HeLa
HGS
STAM
RAB5C
RAB7A
RHOA
UBQLN2
KEAP1
PDCD6IP
PRKAR1A
TNIP1
NDFIP1
SCAMP3
VAPA
VAPB
cargo candidate
LAMP1
cargo candidate
LAMP1

Figure 5

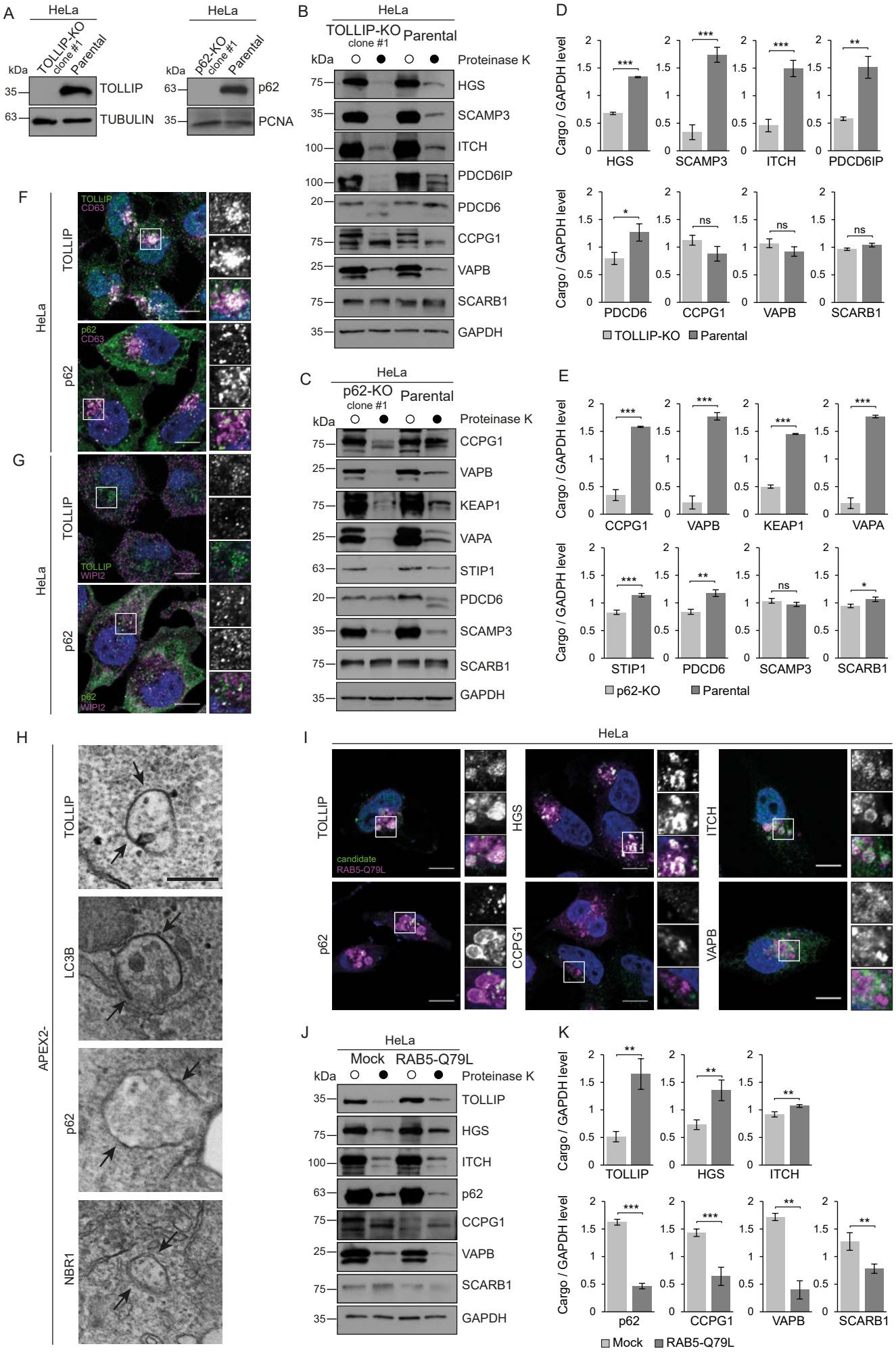
A
HeLa
TOLLIP-KO clone #1
Parental
kDa
35
TOLLIP
63
TUBULIN
HeLa
p62-KO clone #1
Parental
kDa
63
p62
35
PCNA
B
HeLa
TOLLIP-KO clone #1
Parental
kDa
Proteinase K
75
HGS
35
SCAMP3
100
ITCH
100
PDCD6IP
20
PDCD6
75
CCPG1
25
VAPB
75
SCARB1
35
GAPDH
C
HeLa
p62-KO clone #1
Parental
kDa
Proteinase K
75
CCPG1
25
VAPB
75
KEAP1
25
VAPA
63
STIP1
20
PDCD6
35
SCAMP3
75
SCARB1
35
GAPDH
D
Cargo / GAPDH level
HGS
SCAMP3
ITCH
PDCD6IP
PDCD6
CCPG1
VAPB
SCARB1
TOLLIP-KO
Parental
E
Cargo / GAPDH level
CCPG1
VAPB
KEAP1
VAPA
STIP1
PDCD6
SCAMP3
SCARB1
p62-KO
Parental
F
HeLa
TOLLIP
p62
TOLLIP
CD63
p62
CD63
G
HeLa
TOLLIP
p62
TOLLIP
WIPI2
p62
WIPI2
H
APEX2-
TOLLIP
LC3B
p62
NBR1
I
HeLa
TOLLIP
p62
candidate
RAB5-Q79L
HGS
CCPG1
ITCH
VAPB
J
HeLa
Mock
RAB5-Q79L
kDa
Proteinase K
35
TOLLIP
75
HGS
100
ITCH
63
p62
75
CCPG1
25
VAPB
75
SCARB1
35
GAPDH
K
Cargo / GAPDH level
TOLLIP
HGS
ITCH
p62
CCPG1
VAPB
SCARB1
Mock
RAB5-Q79L

Figure 6

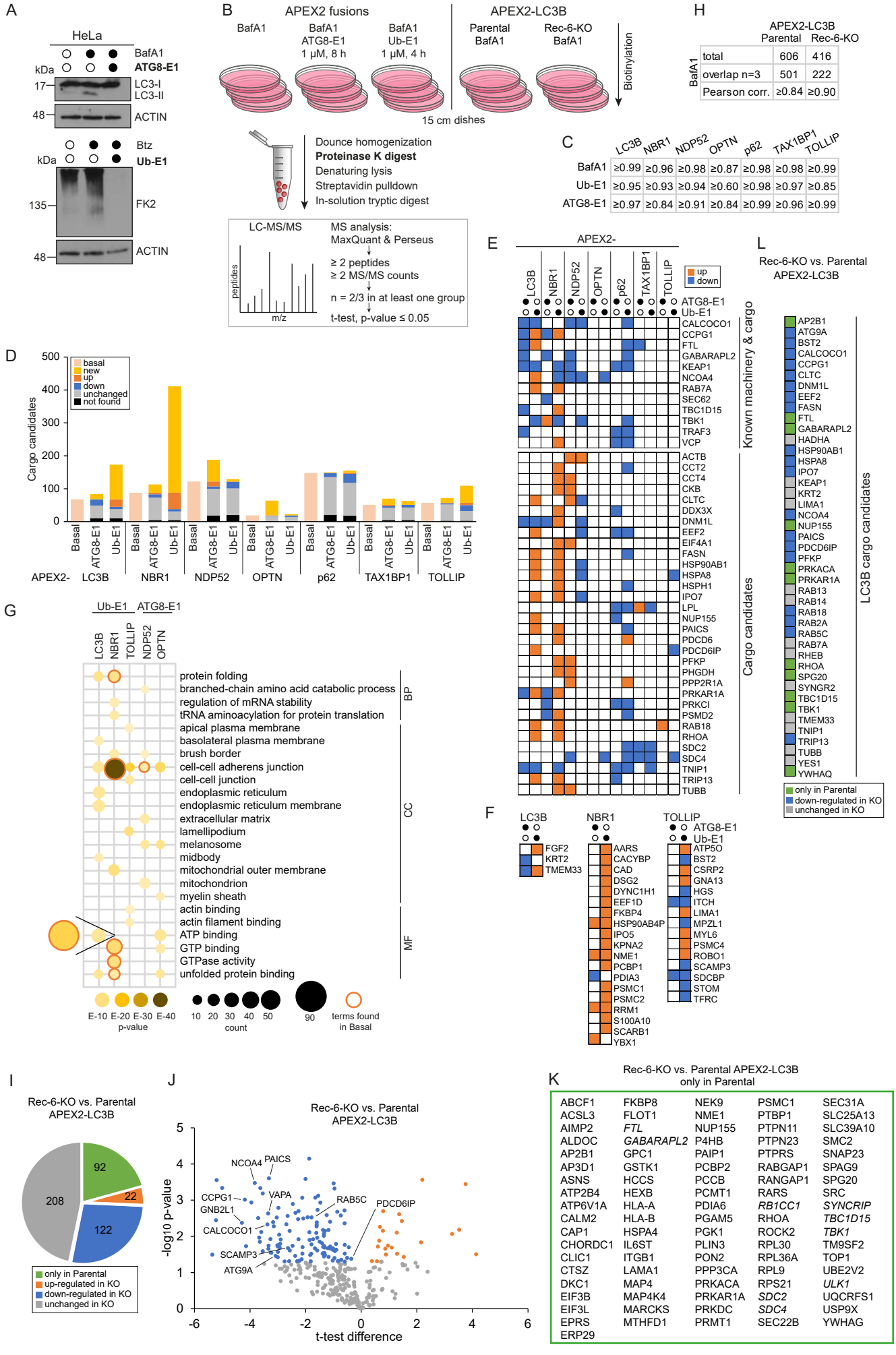
A
HeLa
BafA1
ATG8-E1
kDa
17
LC3-I
LC3-II
48
ACTIN
Btz
Ub-E1
135
FK2
B
APEX2 fusions
BafA1
BafA1 ATG8-E1 1 µM, 8 h
BafA1 Ub-E1 1 µM, 4 h
APEX2-LC3B
Parental BafA1
Rec-6-KO BafA1
Biotinylation
15 cm dishes
Dounce homogenization
Proteinase K digest
Denaturing lysis
Streptavidin pulldown
In-solution tryptic digest
LC-MS/MS
peptides
m/z
MS analysis:
MaxQuant & Perseus
≥ 2 peptides
≥ 2 MS/MS counts
n = 2/3 in at least one group
t-test, p-value ≤ 0.05
H
APEX2-LC3B
Parental Rec-6-KO
BafA1
total 606 416
overlap n=3 501 222
Pearson corr. ≥0.84 ≥0.90
C
LC3B NBR1 NDP52 OPTN p62 TAX1BP1 TOLLIP
BafA1 ≥0.99 ≥0.96 ≥0.98 ≥0.87 ≥0.98 ≥0.98 ≥0.99
Ub-E1 ≥0.95 ≥0.93 ≥0.94 ≥0.60 ≥0.98 ≥0.97 ≥0.85
ATG8-E1 ≥0.97 ≥0.84 ≥0.91 ≥0.84 ≥0.99 ≥0.96 ≥0.99
D
Cargo candidates
basal
new
up
down
unchanged
not found
Basal
ATG8-E1
Ub-E1
APEX2- LC3B NBR1 NDP52 OPTN p62 TAX1BP1 TOLLIP
E
APEX2-
up
down
ATG8-E1
Ub-E1
CALCOCO1
CCPG1
FTL
GABARAPL2
KEAP1
NCOA4
RAB7A
SEC62
TBC1D15
TBK1
TRAF3
VCP
Known machinery & cargo
ACTB
CCT2
CCT4
CKB
CLTC
DDX3X
DNM1L
EEF2
EIF4A1
FASN
HSP90AB1
HSPA8
HSPH1
IPO7
LPL
NUP155
PAICS
PDCD6
PDCD6IP
PFKP
PHGDH
PPP2R1A
PRKAR1A
PRKCI
PSMD2
RAB18
RHOA
SDC2
SDC4
TNIP1
TRIP13
TUBB
Cargo candidates
L
Rec-6-KO vs. Parental
APEX2-LC3B
AP2B1
ATG9A
BST2
CALCOCO1
CCPG1
CLTC
DNM1L
EEF2
FASN
FTL
GABARAPL2
HADHA
HSP90AB1
HSPA8
IPO7
KEAP1
KRT2
LIMA1
NCOA4
NUP155
PAICS
PDCD6IP
PFKP
PRKACA
PRKAR1A
RAB13
RAB14
RAB18
RAB2A
RAB5C
RAB7A
RHEB
RHOA
SPG20
SYNGR2
TBC1D15
TBK1
TMEM33
TNIP1
TRIP13
TUBB
YES1
YWHAQ
LC3B cargo candidates
only in Parental
down-regulated in KO
unchanged in KO
F
LC3B
FGF2
KRT2
TMEM33
NBR1
AARS
CACYBP
CAD
DSG2
DYNC1H1
EEF1D
FKBP4
HSP90AB4P
IPO5
KPNA2
NME1
PCBP1
PDIA3
PSMC1
PSMC2
RRM1
S100A10
SCARB1
YBX1
TOLLIP
ATG8-E1
Ub-E1
ATP5O
BST2
CSRP2
GNA13
HGS
ITCH
LIMA1
MPZL1
MYL6
PSMC4
ROBO1
SCAMP3
SDCBP
STOM
TFRC
G
Ub-E1 ATG8-E1
LC3B NBR1 TOLLIP NDP52 OPTN
protein folding
branched-chain amino acid catabolic process
regulation of mRNA stability
tRNA aminoacylation for protein translation
apical plasma membrane
basolateral plasma membrane
brush border
cell-cell adherens junction
cell-cell junction
endoplasmic reticulum
endoplasmic reticulum membrane
extracellular matrix
lamellipodium
melanosome
midbody
mitochondrial outer membrane
mitochondrion
myelin sheath
actin binding
actin filament binding
ATP binding
GTP binding
GTPase activity
unfolded protein binding
BP
CC
MF
E-10 E-20 E-30 E-40
p-value
10 20 30 40 50
count
90
terms found in Basal
I
Rec-6-KO vs. Parental
APEX2-LC3B
92
22
122
208
only in Parental
up-regulated in KO
down-regulated in KO
unchanged in KO
J
Rec-6-KO vs. Parental
APEX2-LC3B
-log10 p-value
t-test difference
NCOA4
PAICS
CCPG1
GNB2L1
VAPA
RAB5C
PDCD6IP
CALCOCO1
SCAMP3
ATG9A
K
Rec-6-KO vs. Parental APEX2-LC3B
only in Parental
ABCF1 ACSL3 AIMP2 ALDOC AP2B1 AP3D1 ASNS ATP2B4 ATP6V1A CALM2 CAP1 CHORDC1 CLIC1 CTSZ DKC1 EIF3B EIF3L EPRS ERP29
FKBP8 FLOT1 FTL GABARAPL2 GPC1 GSTK1 HCCS HEXB HLA-A HLA-B HSPA4 IL6ST ITGB1 LAMA1 MAP4 MAP4K4 MARCKS MTHFD1
NEK9 NME1 NUP155 P4HB PAIP1 PCBP2 PCCB PCMT1 PDIA6 PGAM5 PGK1 PLIN3 PON2 PPP3CA PRKACA PRKAR1A PRKDC PRMT1
PSMC1 PTBP1 PTPN11 PTPN23 PTPRS RABGAP1 RANGAP1 RARS RB1CC1 RHOA ROCK2 RPL30 RPL36A RPL9 RPS21 SDC2 SDC4 SEC22B
SEC31A SLC25A13 SLC39A10 SMC2 SNAP23 SPAG9 SPG20 SRC SYNCRIP TBC1D15 TBK1 TM9SF2 TOP1 UBE2V2 ULK1 UQCRFS1 USP9X YWHAG

Figure 7

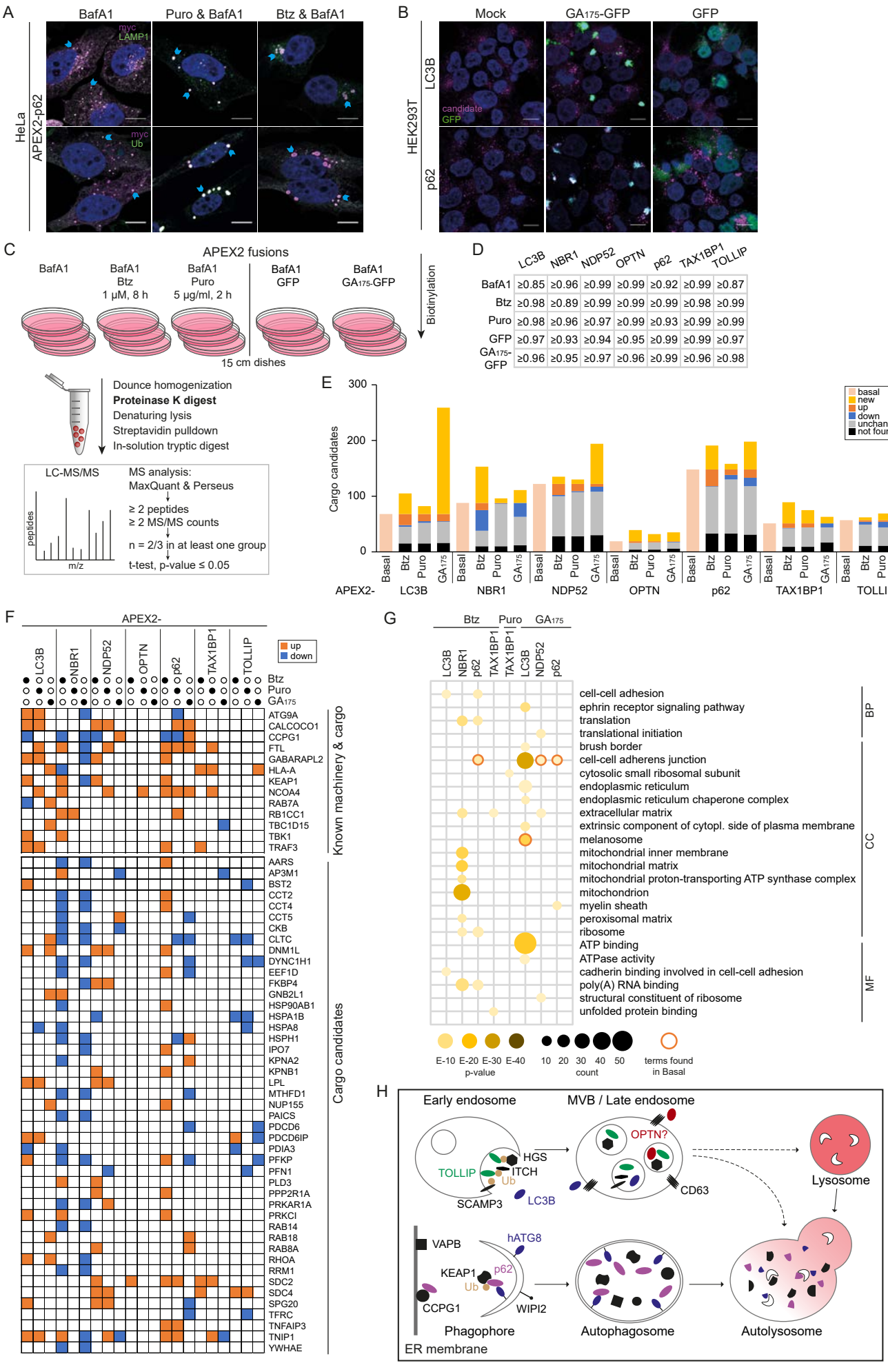
A
BafA1
Puro & BafA1
Btz & BafA1
HeLa
APEX2-p62
myc
LAMP1
myc
Ub
B
Mock
GA175-GFP
GFP
HEK293T
LC3B
p62
candidate
GFP
C
APEX2 fusions
BafA1
BafA1 Btz 1 μM, 8 h
BafA1 Puro 5 μg/ml, 2 h
BafA1 GFP
BafA1 GA175-GFP
Biotinylation
15 cm dishes
Dounce homogenization
Proteinase K digest
Denaturing lysis
Streptavidin pulldown
In-solution tryptic digest
LC-MS/MS
peptides
m/z
MS analysis:
MaxQuant & Perseus
≥ 2 peptides
≥ 2 MS/MS counts
n = 2/3 in at least one group
t-test, p-value ≤ 0.05
D
LC3B NBR1 NDP52 OPTN p62 TAX1BP1 TOLLIP
BafA1 ≥0.85 ≥0.96 ≥0.99 ≥0.99 ≥0.92 ≥0.99 ≥0.87
Btz ≥0.98 ≥0.89 ≥0.99 ≥0.99 ≥0.99 ≥0.98 ≥0.99
Puro ≥0.98 ≥0.96 ≥0.97 ≥0.99 ≥0.93 ≥0.99 ≥0.99
GFP ≥0.97 ≥0.93 ≥0.94 ≥0.95 ≥0.99 ≥0.99 ≥0.97
GA175-GFP ≥0.96 ≥0.95 ≥0.97 ≥0.96 ≥0.99 ≥0.96 ≥0.98
E
Cargo candidates
basal
new
up
down
unchanged
not found
APEX2-
LC3B
NBR1
NDP52
OPTN
p62
TAX1BP1
TOLLIP
F
APEX2-
up
down
Btz
Puro
GA175
Known machinery & cargo
Cargo candidates
ATG9A
CALCOCO1
CCPG1
FTL
GABARAPL2
HLA-A
KEAP1
NCOA4
RAB7A
RB1CC1
TBC1D15
TBK1
TRAF3
AARS
AP3M1
BST2
CCT2
CCT4
CCT5
CKB
CLTC
DNM1L
DYNC1H1
EEF1D
FKBP4
GNB2L1
HSP90AB1
HSPA1B
HSPA8
HSPH1
IPO7
KPNA2
KPNB1
LPL
MTHFD1
NUP155
PAICS
PDCD6
PDCD6IP
PDIA3
PFKP
PFN1
PLD3
PPP2R1A
PRKAR1A
PRKCI
RAB14
RAB18
RAB8A
RHOA
RRM1
SDC2
SDC4
SPG20
TFRC
TNFAIP3
TNIP1
YWHAE
G
Btz
Puro
GA175
cell-cell adhesion
ephrin receptor signaling pathway
translation
translational initiation
brush border
cell-cell adherens junction
cytosolic small ribosomal subunit
endoplasmic reticulum
endoplasmic reticulum chaperone complex
extracellular matrix
extrinsic component of cytopl. side of plasma membrane
melanosome
mitochondrial inner membrane
mitochondrial matrix
mitochondrial proton-transporting ATP synthase complex
mitochondrion
myelin sheath
peroxisomal matrix
ribosome
ATP binding
ATPase activity
cadherin binding involved in cell-cell adhesion
poly(A) RNA binding
structural constituent of ribosome
unfolded protein binding
BP
CC
MF
E-10 E-20 E-30 E-40
p-value
10 20 30 40 50
count
terms found in Basal
H
Early endosome
MVB / Late endosome
TOLLIP
HGS
ITCH
Ub
SCAMP3
LC3B
OPTN?
CD63
Lysosome
VAPB
hATG8
KEAP1
p62
Ub
CCPG1
WIPI2
Phagophore
Autophagosome
Autolysosome
ER membrane

Figure S1. Expression and localization of APEX2 baits, Related to Figure 1

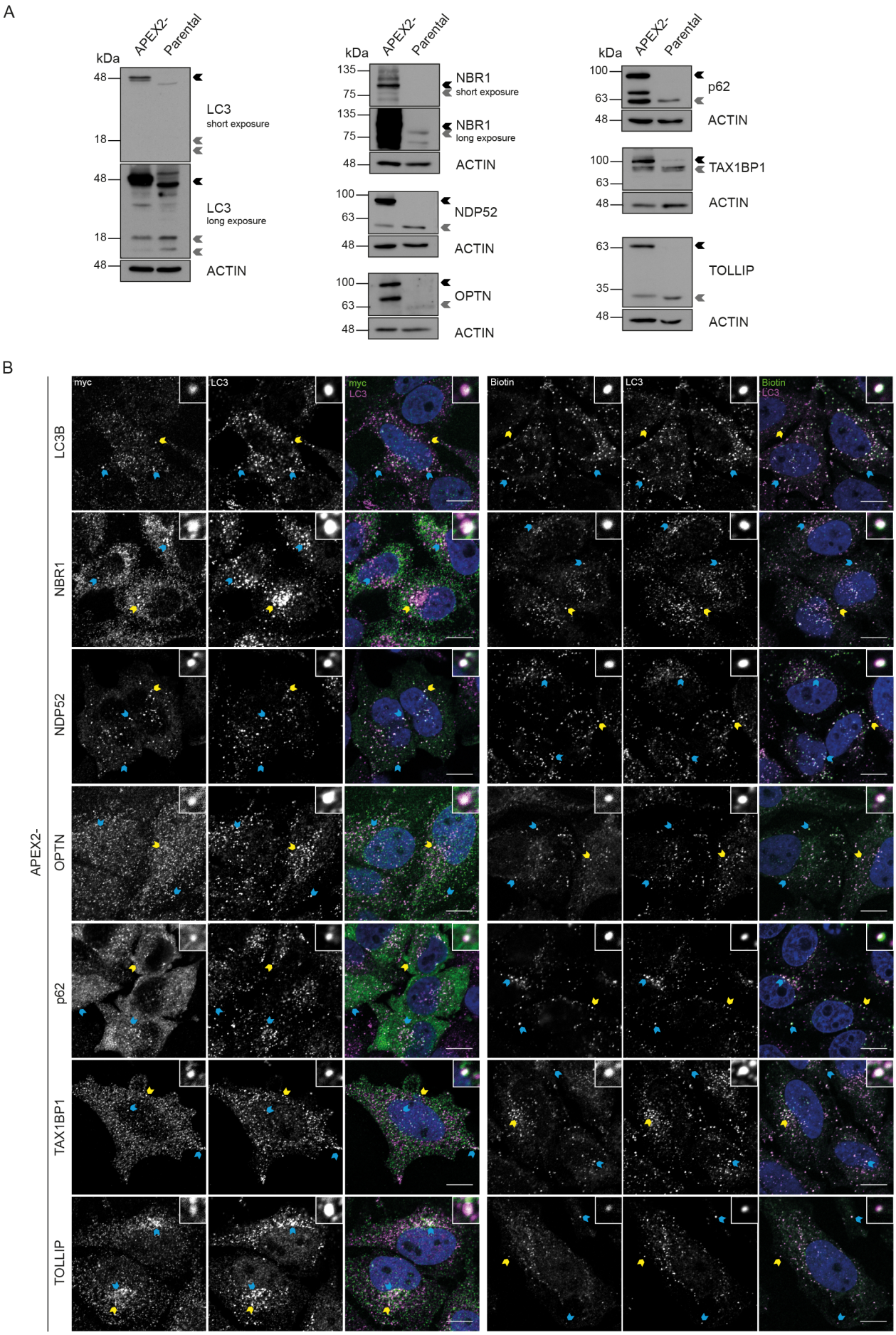

Figure S2. Benchmarking protease protection coupled proximity profiling, Related to Figure 2

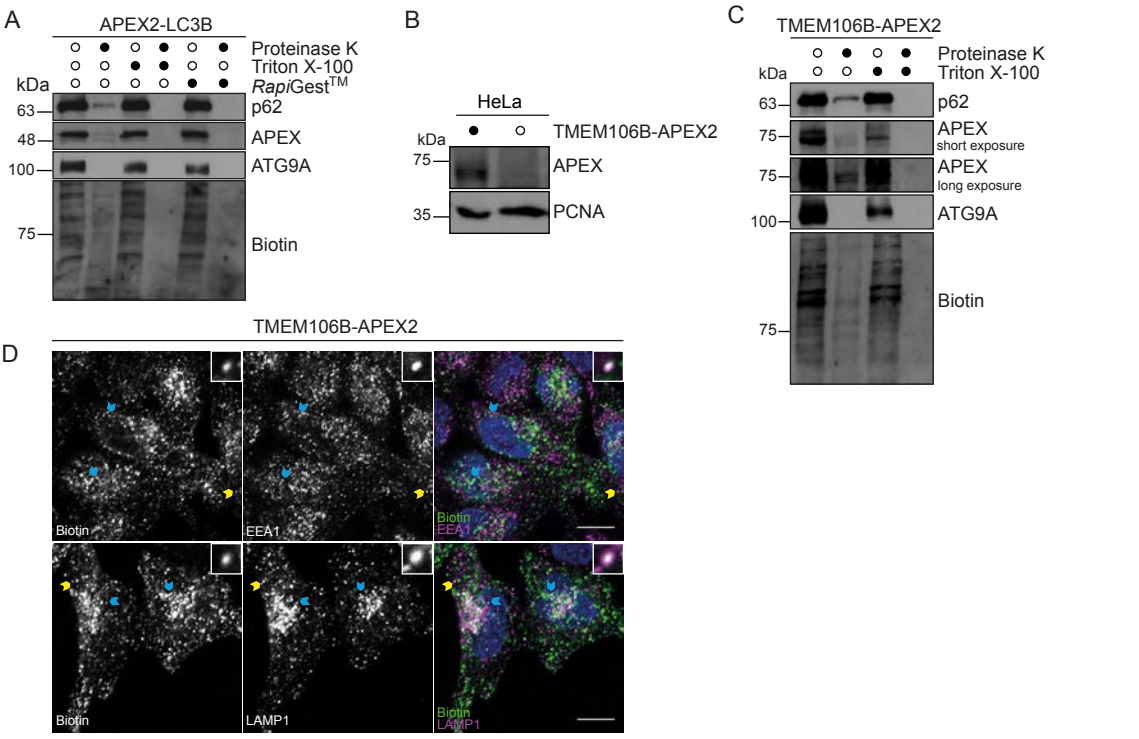

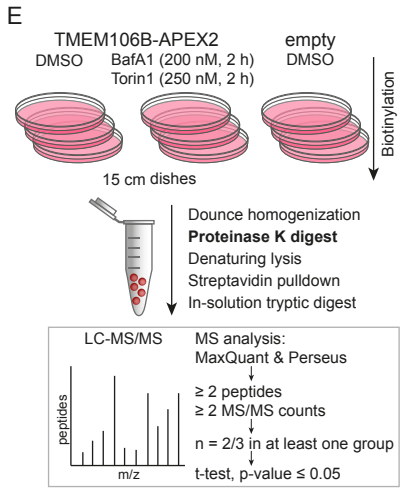

F

TMEM106B-APEX2

DMSO	overlap n=3	445
	total	582
	Pearson corr.	≥0.99
BafA1 Torin1	overlap n=3	514
	total	555
	Pearson corr.	≥0.97
HeLa	overlap n=3	188
	total	349
	Pearson corr.	≥0.99

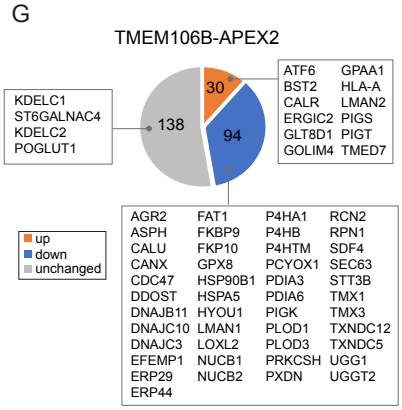

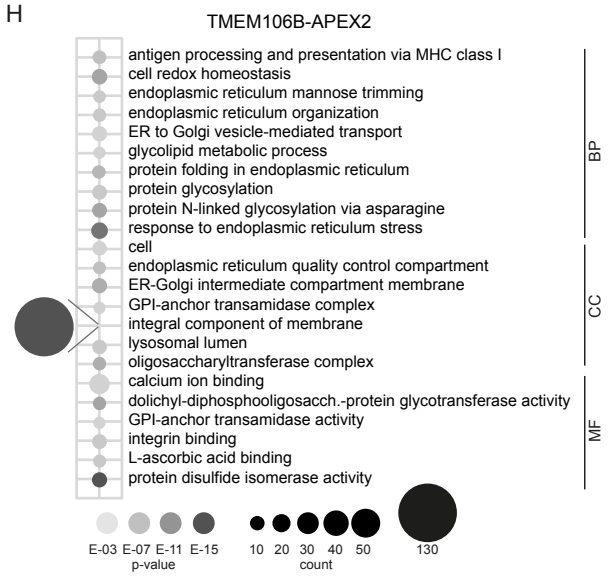

I

		LC3B	NBR1	NDP52	OPTN	p62	TAX1BP1	TOLLIP
DMSO	overlap n=3	336	474	403	360	726	325	300
	total	640	699	657	626	868	690	525
BafA1	overlap n=3	400	448	489	353	658	541	337
	total	619	706	777	661	900	783	577

Figure S3. Shared and unique degradative autophagy cargo candidates, Related to Figure 2

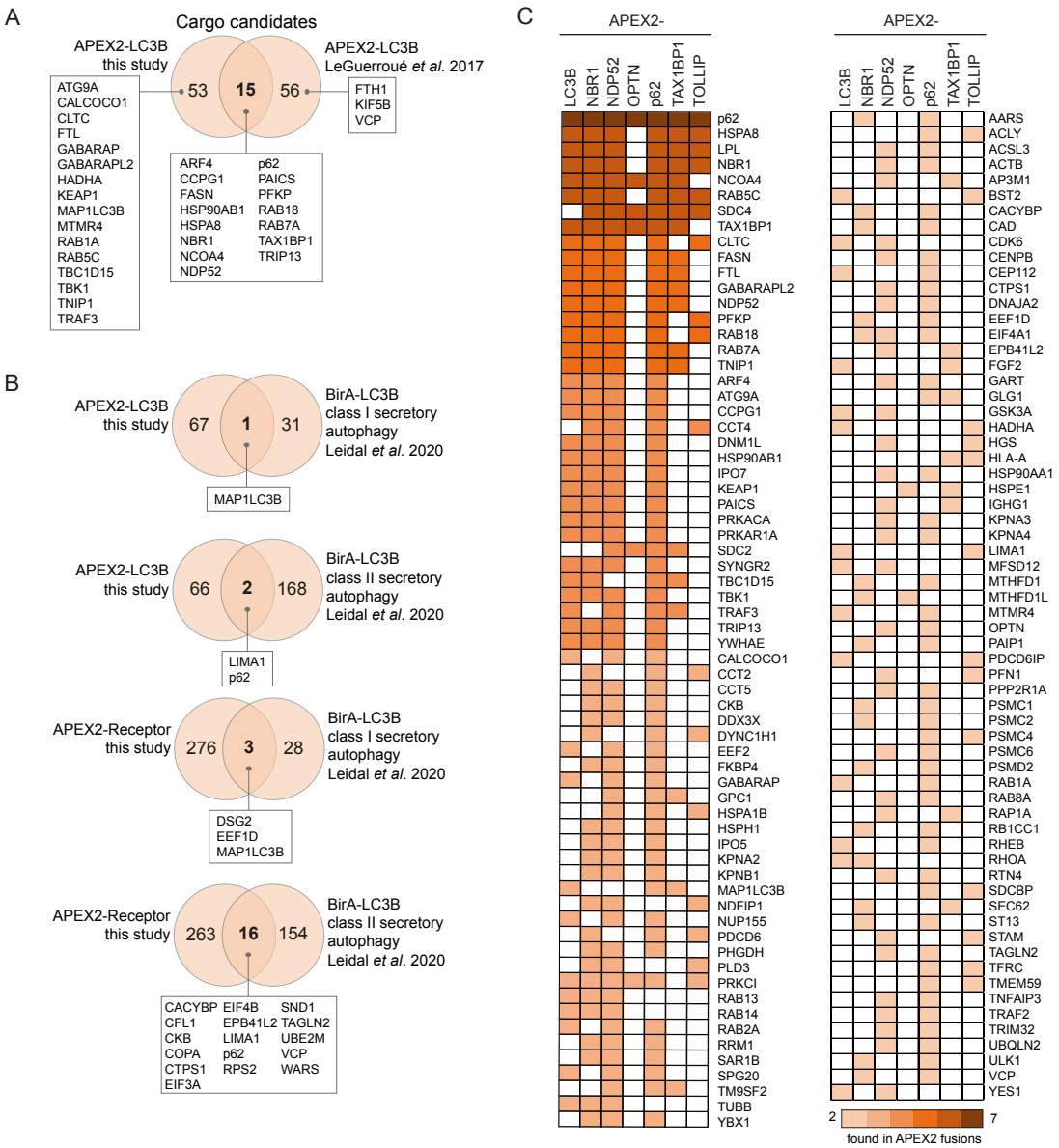

D

Unique Hits

LC3B	NBR1	NDP52	OPTN	p62	TAX1BP1	TOLLIP
AP2B1	ACTR2	ATP6V0D1	AFG3L2	ATP2A2	ACAT1	ANTXR1
AP2M1	CKAP4	BASP1	COL18A1	BZW1	CISD2	ATP1A1
B2M	DSG2	CAV1	DARS2	CCAR2	CNN2	ATP5O
CSTA	G6PD	CDC42	EIF5A	CCT3	COL12A1	CLU
CYFIP1	GIPC1	CFL1	GNAI3	CCT6A	DEK	COLGALT1
EPHB4	GLS	CKM	HEXA	CCT7	ERLIN2	CSRP2
KRT2	GNB2L1	CNOT1	HSPD1	CSNK2A1	FKBP10	FARSB
TMEM33	GSTM3	COPA	NLE1	EIF2S3	HADHB	GNA13
TPP2	HSP90AB4P	CSNK2B	PCBP2	EIF3A	HCCS	GNAI2
UBE2D2	IGF2R	CTSB	SRP9	EIF4B	HNRNPA3	GRSF1
	LGALS1	EEF1G	WARS	ERLIN1	LAMA5	HSP90B1
	MRPL3	FLNB		FASTKD2	MARCKS	ITCH
	NME1	GDA		HEXB	NADK2	ITGB1
	PCBP1	HNRNPA1		HIST1H2BN	NOTCH2	KIF23
	S100A10	LANCL1		HMGB1	NSDHL	LYN
	SCARB1	LIN7C		HSPA4	PEG10	MCCC2
	VANGL1	MT-CO2		IMPDH2	PIGT	MDH2
		NRD1		KLHL8	POLRMT	MPZL1
		PPIA		LRRC59	RPS12	MYL6
		PPP1CA		MAT2A	RPS16	PDIA3
		PPP1CB		MFF	THEM6	ROBO1
		PRPF19		MFN2	TOP1	RPS27
		RHOG		NPR3		SCAMP3
		RPL17		PABPC1		SLC2A1
		RPS2		PFKM		SNAP23
		SLC1A5		PGD		STOM
		SPECC1		PSMC3		THOP1
		SRRM2		PSMC5		
		UBE2M		RAB21		
				RPS17		
				S100A6		
				SEPT7		
				SMC4		
				SND1		
				STIP1		
				TCP1		
				TNPO1		
				TPP1		
				TUBB4B		
				VAPA		
				VAPB		
				XPO1		
				YWHAB		

Figure S4. Identification of proximity partners of SLRs, Related to Figure 3

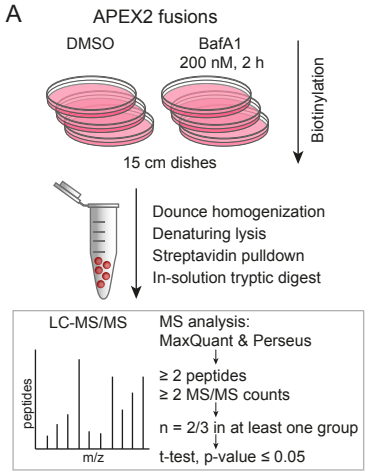

B

		LC3B	NBR1	NDP52	OPTN	p62	TAX1BP1	TOLLIP	LC3B no BP	Parental
DMSO	total	2860	2913	2819	2911	2923	2875	3041	2813	2961
	overlap n=3	2236	2400	2371	2362	2321	2262	2576	2173	2410
	Pearson corr.	≥0.93	≥0.99	≥0.95	≥0.99	≥0.96	≥0.98	≥0.98	≥0.97	≥0.99
BafA1	total	2766	2868	2910	2915	3010	2850	2985	2844	
	overlap n=3	2143	2309	2365	2415	2312	2453	2516	2294	
	Pearson corr.	≥0.94	≥0.91	≥0.99	≥0.99	≥0.97	≥0.96	≥0.95	≥0.99	

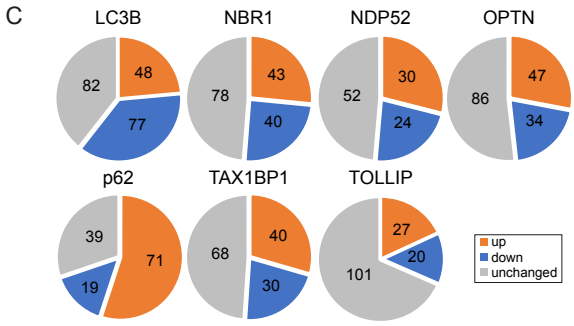

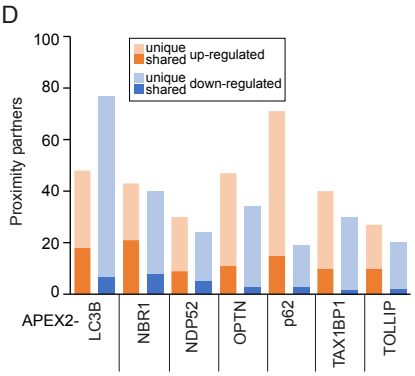

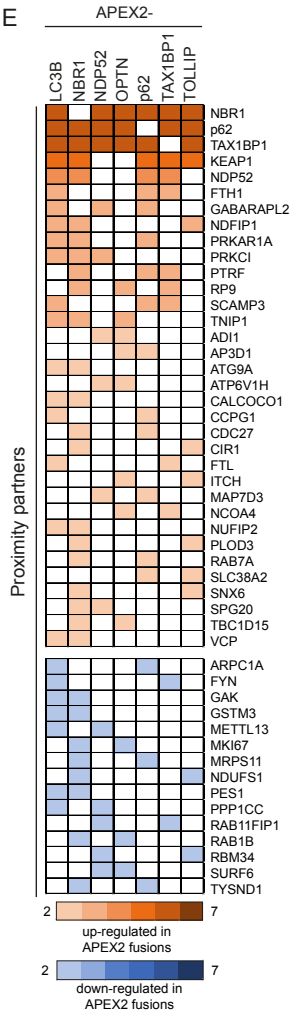

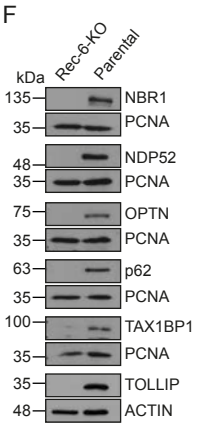

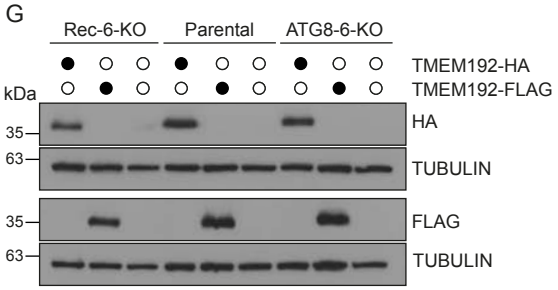

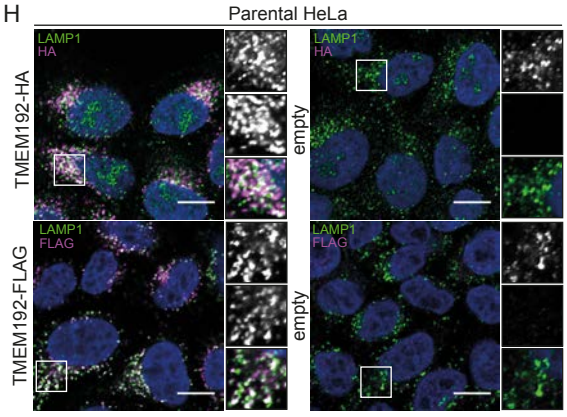

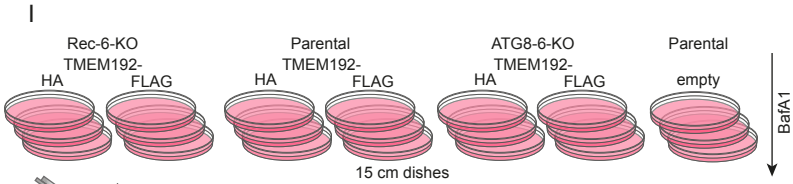

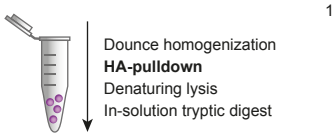

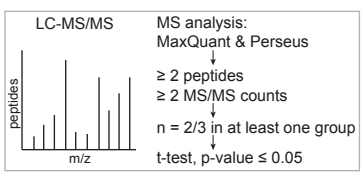

J

	Rec-6-KO TMEM192-HA	Rec-6-KO TMEM192-FLAG	Parental TMEM192-HA	Parental TMEM192-FLAG	ATG8-6-KO TMEM192-HA	ATG8-6-KO TMEM192-FLAG	Parental empty
total	3496	3412	3363	3168	3461	3428	3443
overlap n=3	2935	2661	2448	2377	2948	2749	2616
Pearson corr.	≥0.97	≥0.85	≥0.93	≥0.96	≥0.98	≥0.98	≥0.83

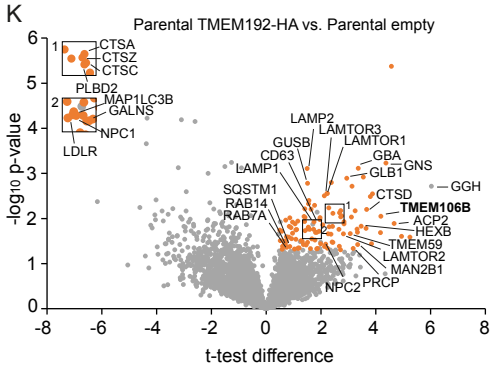

Figure S5. Extended validation of SLR cargo candidates, Related to Figure 4

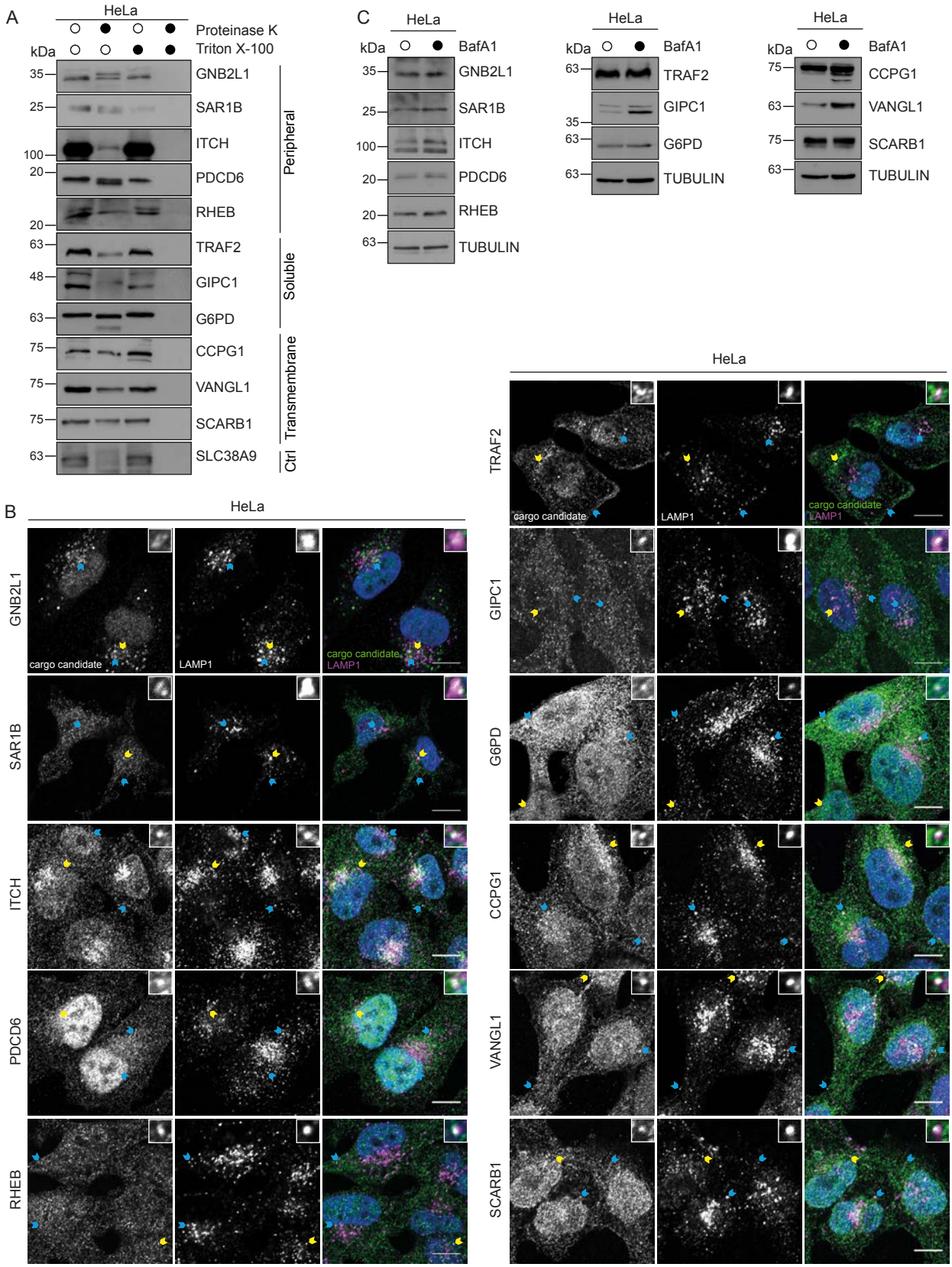

Figure S6. Endosomal localization of distinct SLRs and cargo candidates, Related to Figure 5

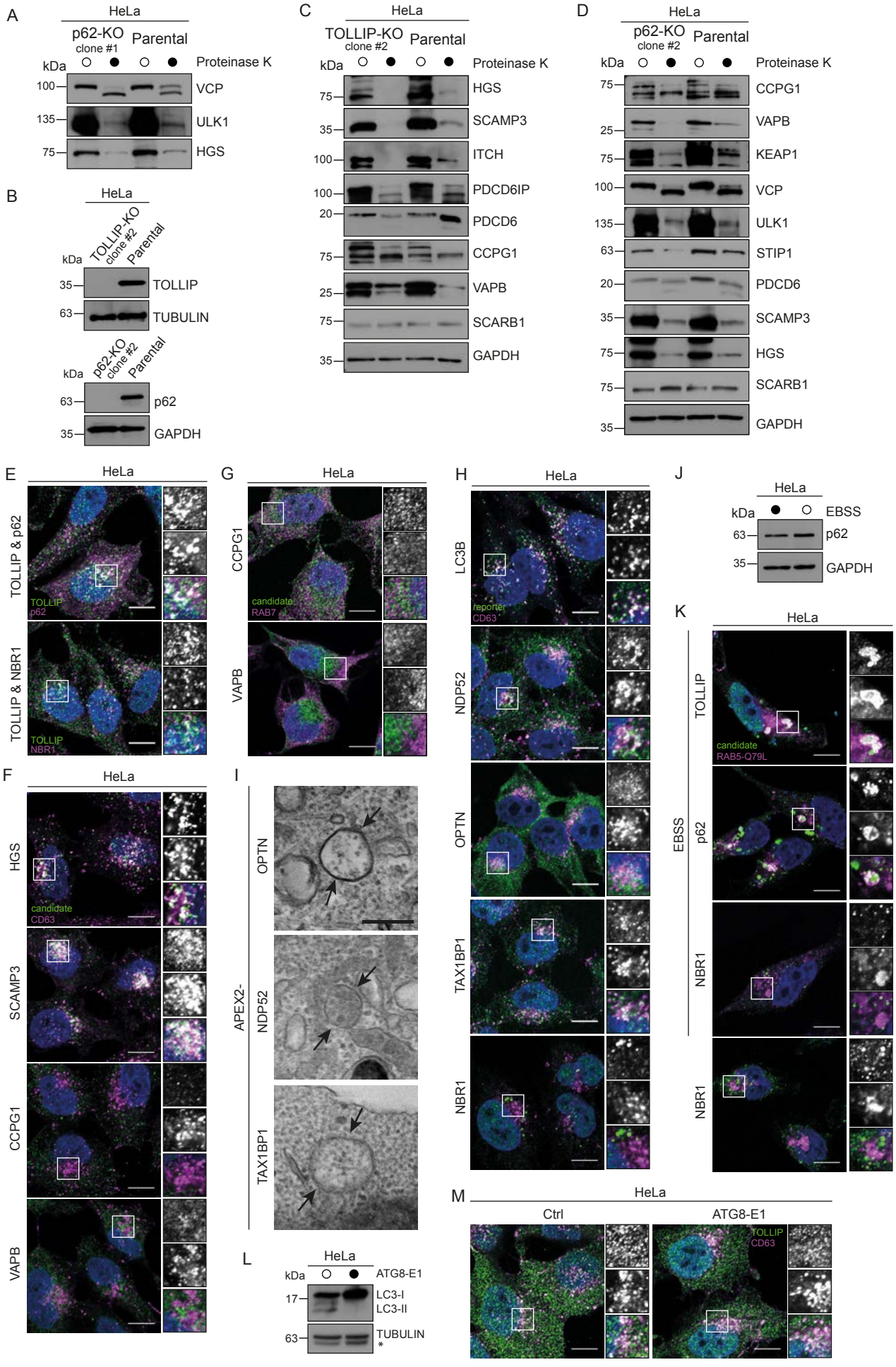

Figure S7. Lysosomal delivery of TOLLIP cargo via endosomal microautophagy, Related to Figure 5

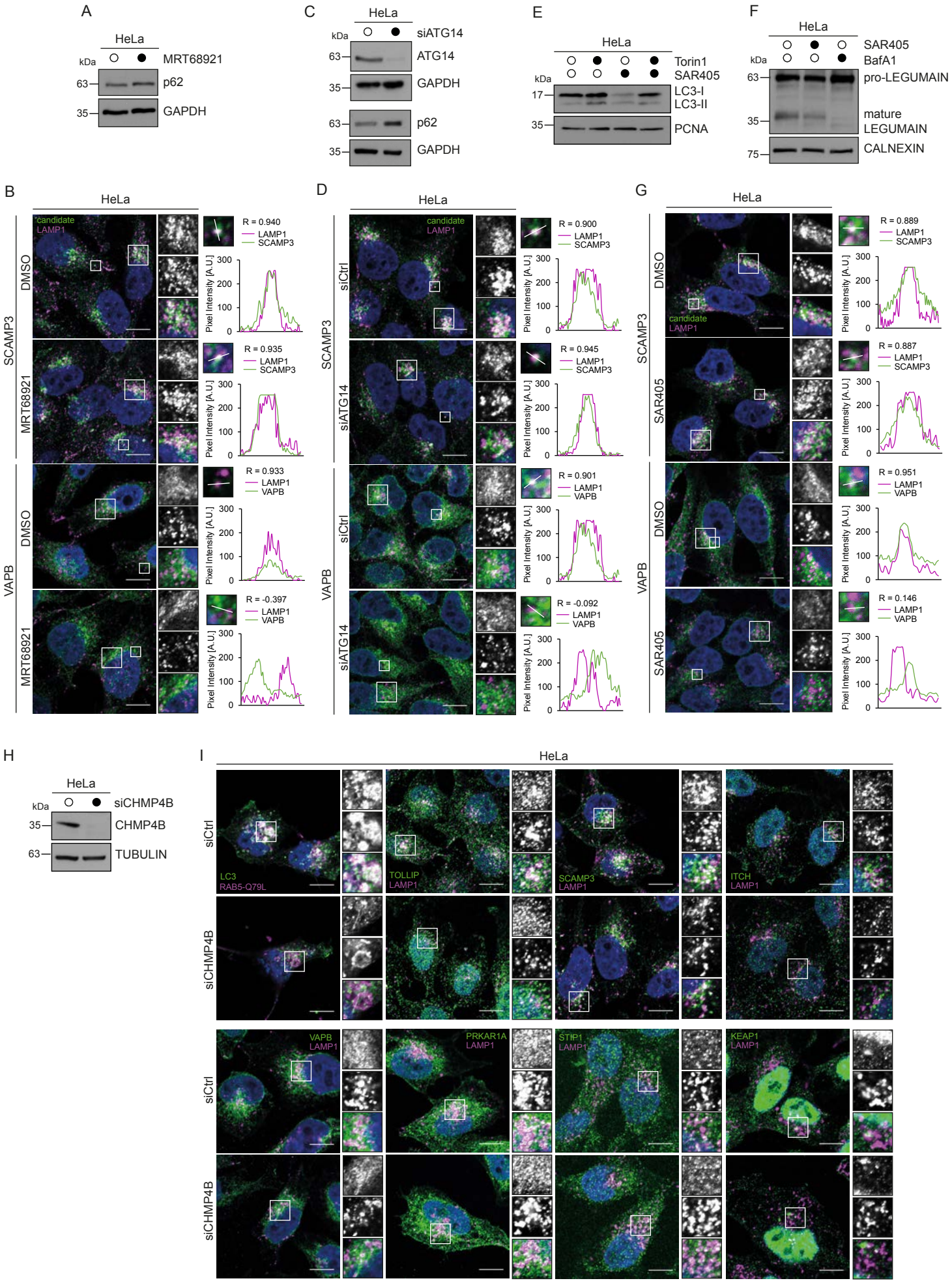

Figure S8. Dependence of cargo engulfment on ubiquitination and hATG8 lipidation, Related to Figure 5, 6 and 7

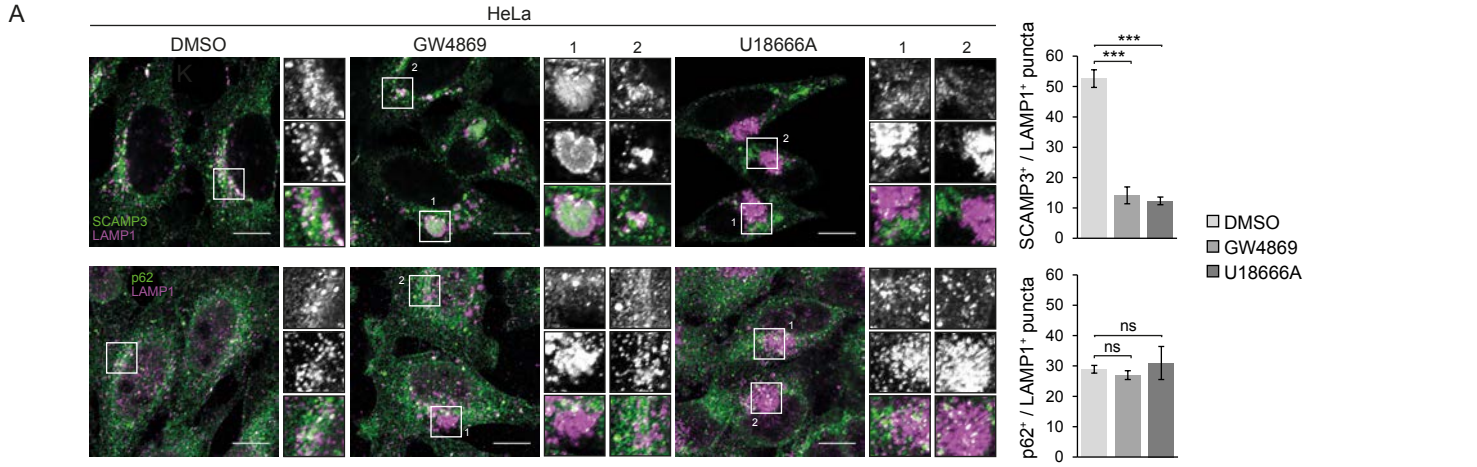

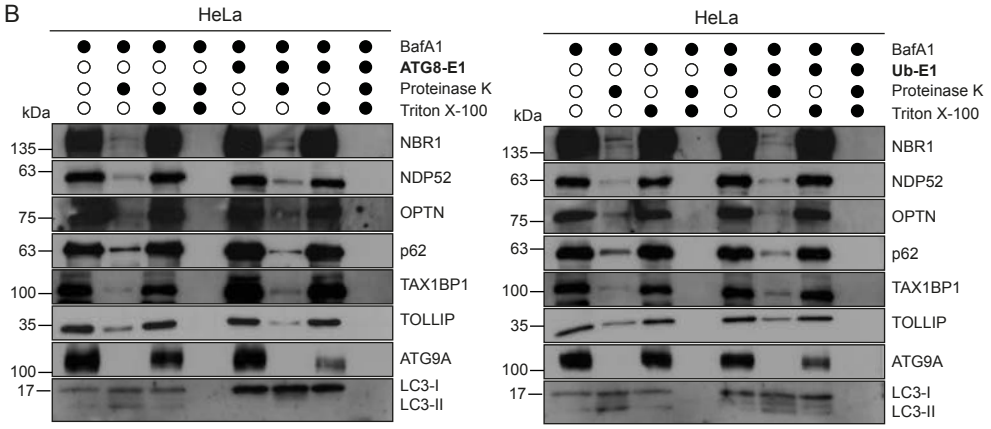

C

		LC3B	NBR1	NDP52	OPTN	p62	TAX1BP1	TOLLIP
BafA1	total	521	735	402	443	608	413	673
	overlap n=3	277	399	176	214	373	212	428
Ub-E1	total	667	926	385	555	566	409	747
	overlap n=3	442	783	97	149	248	221	438
ATG8-E1	total	401	720	746	610	571	428	670
	overlap n=3	179	450	289	241	323	199	314

D

APEX2-LC3B
ER-associated proteins after Ub-E1 treatment

ACSL3	FKBP4	RCN1
ACSL4	HLA-A	RPN1
ASS1	HSP90B1	SEC62
ATL3	LPCAT1	SERPINH1
ATP1A1	LRRC59	SPTLC1
ATP2A2	MARCH5	TAPBP
CDC42	NOTCH2	TECR
COPA	PDCD6	TXNDC5
EEF1D	PDIA3	VAPA
EGFR	PTGS2	

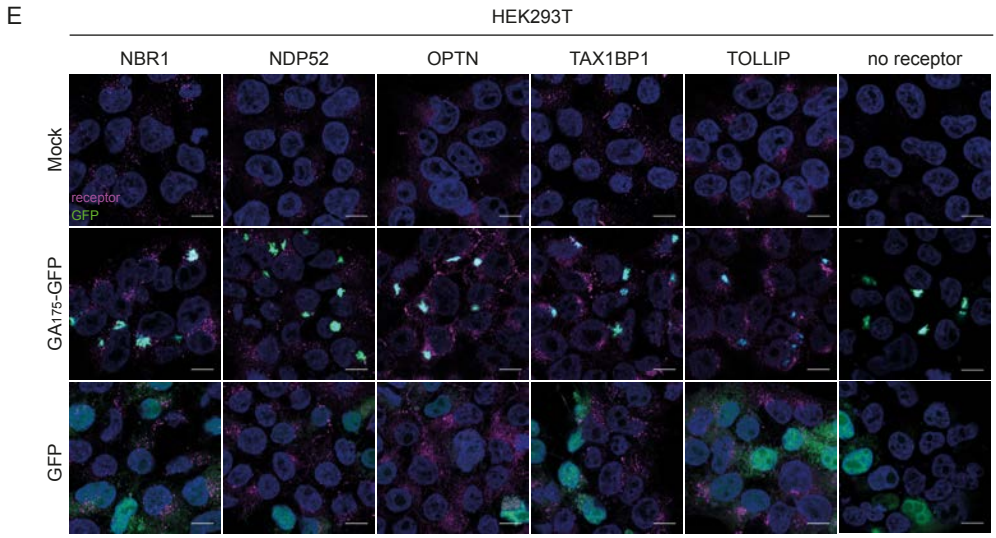

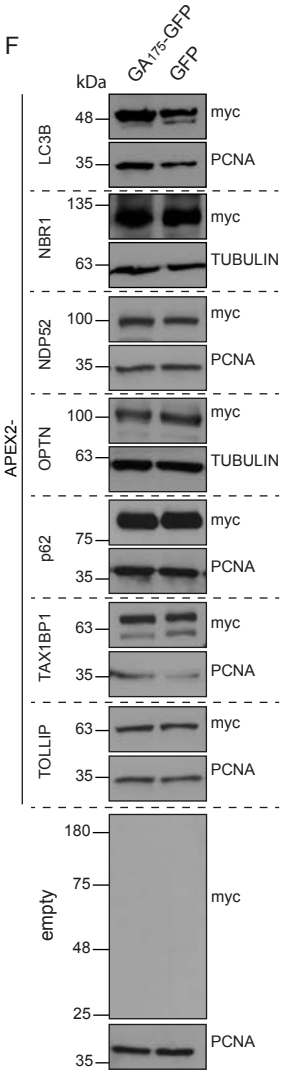

G

		LC3B	NBR1	NDP52	OPTN	p62	TAX1BP1	TOLLIP
BafA1	total	618	641	518	442	582	566	433
	overlap n=3	431	486	317	199	370	363	213
Btz	total	649	710	455	387	556	536	463
	overlap n=3	474	602	254	174	363	284	253
Puro	total	643	638	517	434	622	512	457
	overlap n=3	502	498	311	136	421	324	253
GFP	total	912	1024	1113	1007	1216	1066	1342
	overlap n=3	595	700	724	730	901	814	1115
GA175-GFP	total	1095	921	1120	958	1141	927	1301
	overlap n=3	752	525	771	638	803	545	1040

H

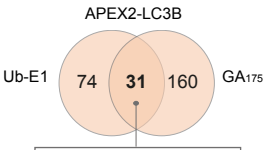

ACLY	FKBP4	ROR2
ACSL4	HLA-A	RRAS2
ANXA11	HSP90B1	SLC25A6
ATP1A1	HSPA1B	SLC3A2
ATP2A2	HSPH1	SNAP23
ATP6V0D1	IQGAP1	TFRC
CAD	ITGB1	UQCRC1
CPNE3	LRRC59	VAPA
CTNNB1	LYN	VIM
CTNND1	PDIA3	
ESYT1	PRKAG1	

Figure S9. Cargo content changes under proteostasis challenging conditions, Related to Figure 7

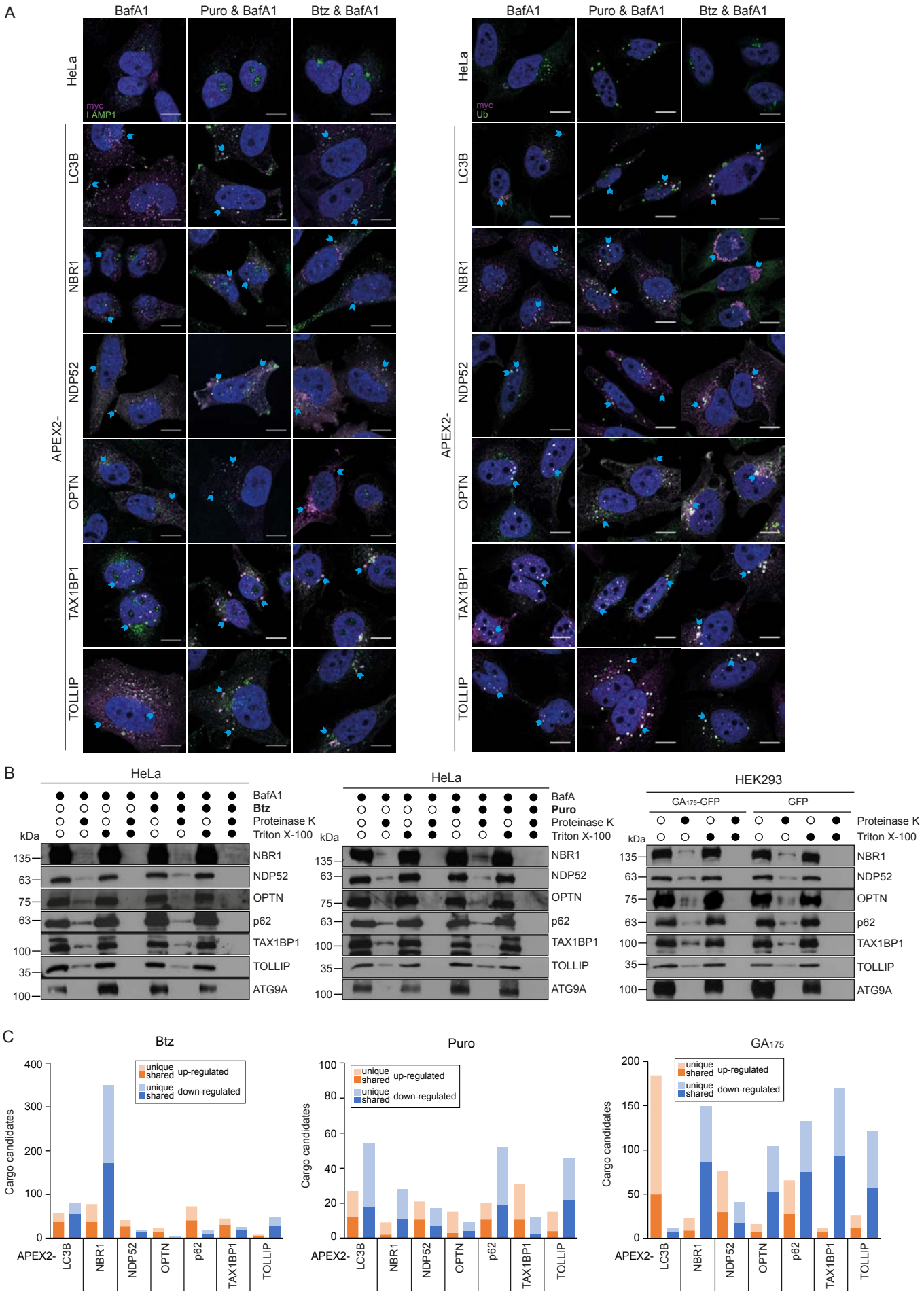

Supplemental Figures

Figure S1. Expression and localization of APEX2 baits, Related to Figure 1

(A) Lysates from parental or APEX2 fusion expressing HeLa cells were analyzed by immunoblotting. Arrowheads indicate endogenous (grey) and overexpressed (black) SLRs and LC3B. (B) APEX2 bait expressing HeLa cells were treated for 2 h with BafA1, 30 min with biotin-phenol and 1 min with H_2O_2 followed by fixation and staining for myc, biotin and LC3. Scale bars, 10 µm. Co-localization events are indicated by blue and yellow arrowheads. Insets show co-localizations of yellow arrowheads.

Figure S2. Benchmarking protease protection coupled proximity profiling, Related to Figure 2

(A) Homogenates from APEX2-LC3B HeLa cells treated for 2 h with BafA1 were incubated with proteinase K and/or Triton X-100 or *RAPI*Gest™ and analyzed by immunoblotting. (B) Lysates from empty and TMEM106B-APEX2 expressing HeLa cells were subjected to immunoblotting with an anti-APEX antibody. (C) Homogenates from TMEM106B-APEX2 HeLa cells treated for 2 h with BafA1, were incubated with proteinase K, Triton X-100 or both prior to immunoblotting. (D) TMEM106B-APEX2 HeLa cells treated for 2 h with BafA1 and Torin1 were fixed and stained with biotin, EEA1 and LAMP1. Scale bars, 10 µm. Co-localization events are indicated by blue and yellow arrowheads. Insets show co-localizations of yellow arrowheads. (E) Schematic overview of protease protection coupled proximity proteomics in TMEM106B-APEX2 HeLa cells. (F) Total and overlapping number of identified proteins as well as Pearson's correlations for 3 biological replicates of TMEM106B-APEX2 profiling. (G) Overview of membrane protected and streptavidin enriched TMEM106B proximal proteins with increased (up), decreased (down) or unchanged abundance upon BafA1/Torin1 treatment. Boxes show examples of each category. (H) GO term enrichment of proteins found by TMEM106B proximity proteomics. BP, biological process, CC, cellular component, MF, molecular function. (I) Overlapping and total number of 3 biological replicates of SLR and LC3B directed autophagosome content profiling.

Figure S3. Shared and unique degradative autophagy cargo candidates, Related to Figure 2

(A) Comparison of APEX2-LC3B cargo candidates identified with the improved new (this study) and previously established protocol (Le Guerroue et al., 2017). (B) Overlap of cargo candidates found in this study with APEX2-LC3B or -SLRs compared to 2 classes of recently identified secretory autophagy proteins (Leidal et al., 2020). (C) Heatmap representation of cargo candidates identified by at least 2 APEX2 baits. (D) Overview of cargo candidates uniquely found by a single APEX2 bait.

Figure S4. Identification of proximity partners of SLRs, Related to Figure 3

(A) Workflow for proximity profiling-based interaction proteomics for SLRs and LC3B. (B) Total and overlapping number of identified proteins as well as Pearson's correlations for 3 biological replicates of proximity interactomics. (C) Overview of proximity partners with increased (up), decreased (down) or unchanged abundance upon BafA1 treatment. (D) Numbers of shared and unique significantly altered proximity partners identified by different APEX2 baits. (E) Heatmap representation of proximity partners identified by at least 2 APEX2 baits. (F) Immunoblotting of lysates from parental and Rec-6-KO HeLa cells. (G) Immunoblot analysis of empty, TMEM192-HA or -FLAG expressing parental, Rec-6-KO or ATG8-6-KO cells. (H) Empty, TMEM192-HA or -FLAG expressing parental HeLa cells were fixed and stained with indicated antibodies or DAPI. Scale bars, 10 µm. Insets show magnifications of boxed areas. (I) Workflow for LysoIP proteomics in parental, Rec-6-KO or ATG8-6-KO cells. (J) Total and overlapping number of identified proteins as well as Pearson's correlations for triplicate LysoIPs. (K) Volcano plot of proteins identified by LysoIPs from empty and TMEM192-HA expressing parental HeLa cells. Significantly altered proteins shown in orange (p-value > 0.05, student's *t*-test) represent lysosomal proteins. Boxes show zooms into the data cloud.

Figure S5. Extended validation of SLR cargo candidates, Related to Figure 4

(A,B) HeLa cells were treated for 2 h with BafA1 followed by homogenization (A) or fixation (B). Homogenates were incubated with either proteinase K, Triton X-100 or both and examined by immunoblot analysis (A). Fixed cells were stained with indicated antibodies and DAPI (B). Scale bars, 10 µm. Co-localization events are indicated by blue and yellow arrowheads. Insets show co-localizations of yellow arrowheads. (C) Lysates from HeLa cells grown for 2 h in the absence or presence of BafA1 were analyzed by immunoblotting.

Figure S6. Endosomal localization of distinct SLRs and cargo candidates, Related to Figure 5

(A) Homogenates from clonal p62 KOs (#1) and parental HeLa cells were left untreated or incubated with proteinase K and immunoblotted for VCP, ULK1 and HGS. (B) Lysates from clonal TOLLIP (#2) and p62 (#2) KOs as well as from parental HeLa cells were analyzed by immunoblotting. (C,D) Homogenates from clonal TOLLIP (C) and p62 KOs (D) as well as parental cells were left untreated or incubated with proteinase K and subjected to immunoblotting. GAPDH served as control. (E-H) HeLa cells treated with BafA1 (E,F,H) or left untreated (G) were fixed and stained for TOLLIP together with p62 or NBR1 (E), CD63 together with HGS, SCAMP3, CCPG1 or VAPB (F), RAB7 together with CCPG1 or VAPB (G) or CD63 together with LC3B, NDP52, OPTN, TAX1BP1 or NBR1. Scale bars, 10 µm. Insets show single and merged channel magnifications of boxed areas. (I) Electron micrographs of indicated APEX2 fusion expressing HeLa cells treated with BafA1. Upon fixation, cells were incubated with DAB and H_2O_2 followed by standard embedding and ultrathin sectioning. Scale bars, 250 nm. (J) Lysates from fed or starved (2 h EBSS) HeLa cells were blotted for p62. (K) HeLa cells expressing mCherry-RAB5-Q79L were fed or starved (EBSS) for 2 h prior to fixation and staining with indicated antibodies and DAPI. Scale bars, 10 µm. Insets show single and merged channel magnifications of boxed areas. (L, M) HeLa cells treated with DMSO or ATG8-E1 were either lysed and blotted for LC3 (L) or fixed and stained with TOLLIP and CD63 (M). Scale

bars, 10 μm. Insets show single and merged channel magnifications of boxed areas. Representative images and immuoblots of two biological replicates are shown.

Figure S7. Lysosomal delivery of TOLLIP cargo via endosomal microautophagy, Related to Figure 5

(A, B) HeLa cells treated with MRT68921 or left untreated were either lysed and immunoblotted for p62 (A) or fixed and stained for LAMP1 together with SCAMP3 or VAPB (B). Scale bars, 10 μm. Insets show single and merged channel magnifications of large boxed areas. Line graphs show pixel intensities measured along a line in the small boxed areas in the merged images. A.U., arbitrary units. *R*, Pearson's correlation coefficient. (C,D) HeLa cells transfected with siCtrl or siATG14 were either lysed and immunoblotted for ATG14 and p62 (C) or fixed and stained for LAMP1 together with SCAMP3 or VAPB (D). Scale bars, 10 μm. Insets show single and merged channel magnifications of large boxed areas. Line graphs show pixel intensities measured along a line in the small boxed areas in the merged images. A.U., arbitrary units. *R*, Pearson's correlation coefficient. (E, F, G) HeLa cells treated with SAR405, BafA1, both or left untreated were either lysed and immunoblotted for LC3 (E) and Legumain (F) or fixed and stained for LAMP1 together with SCAMP3 or VAPB (G). Scale bars, 10 μm. Insets show single and merged channel magnifications of large boxed areas. Line graphs show pixel intensities measured along a line in the small boxed areas in the merged images. A.U., arbitrary units. *R*, Pearson's correlation coefficient. (H) HeLa cells transfected with siCtrl or siCHMP4B were lysed and immunoblotted for CHMP4B. (I) Transiently mCherry-RAB5-Q79L expressing or empty HeLa cells were transfected with siCtrl or siCHMP4B followed by fixation and staining for LC3 only or for LAMP1 in combination with TOLLIP, SCAMP3, ITCH, VAPB, PRKAR1A, STIP1 or KEAP1. Scale bars, 10 μm. Insets show single and merged channel magnifications of boxed areas. Representative images and immuoblots of two biological replicates are shown.

Figure S8. Dependence of cargo engulfment on ubiquitination and hATG8 lipidation, Related to Figure 5, 6 and 7

(A) HeLa cells treated with GW4869, U18666A or left untreated were fixed and stained for LAMP1 and SCAMP3 or p62. Scale bars, 10 μm. Insets show single and merged channel magnifications of boxed areas. Quantification of LAMP1 and SCAMP3 as well as LAMP1 and p62 positive puncta for a total of 540 cells. Data represents mean ± SD of three biological replicates and significance was calculated with Python (student's *t*-test, p-value ≤ 0.05). (B) Homogenates from HeLa cells treated with BafA1 and ATG8-E1 or Ub-E1 were incubated with either proteinase K, Triton X-100 or both followed by immunoblotting with indicated antibodies. (C) Overlapping and total number of identified proteins in 3 biological replicates of autophagosome content profiling upon ATG8-E1 or Ub-E1 treatment. (D) Overview of Ub-E1 induced APEX2-LC3B cargo candidates with GO term associations to the ER. (E) Mock, GFP and GA_{175}-GFP transfected HEK293T cells treated with BafA1 were fixed and stained with indicated antibodies and DAPI. Scale bars, 10 μm. (F) Immunoblot analysis of stable APEX2 fusion expressing HEK293T GFP or GA_{175}-GFP cells treated with BafA1 and tetracycline. (G) Overlapping and total number of identified proteins in 3 biological replicates of autophagosome content profiling upon Btz, Puro or GA_{175} treatment. (H) Comparison of cargo candidates identified with APEX2-LC3B in response to Ub-E1 and GA_{175} conditions.

Figure S9. Cargo content changes under proteostasis challenging conditions, Related to Figure 7

(A) Empty or APEX2 fusion expressing HeLa cells treated for 2 h with BafA1 and/or Puro or Btz were fixed and subjected to staining with indicated antibodies. Scale bars, 10 μm. (B) Homogenates from HeLa cells treated with BafA1 and/or Btz or Puro and from GFP or GA_{175}-GFP expressing HEK293T cells grown in the presence of BafA1 were incubated with either proteinase K, Triton X-100 or both followed by immunoblotting with indicated antibodies. (C) Numbers of shared and unique significantly altered cargo candidates identified by different APEX2 baits.